

Saturn's Probable Interior: An Exploration of Saturn's Potential Interior Density Structures

Naor Movshovitz¹, Jonathan J. Fortney¹, Chris Mankovich^{1,4}, Daniel Thorngren^{2,5}, and Ravit Helled³, Department of Astronomy and Astrophysics, University of California, Santa Cruz, CA, USA; nmovshov@ucsc.edu

Department of Physics, University of California, Santa Cruz, CA, USA; nmovshov@ucsc.edu

Department of Physics, University of California, Santa Cruz, CA, USA

Institute for Computational Science, Center for Theoretical Astrophysics & Cosmology, University of Zurich, Switzerland

Division of Geological and Planetary Sciences, Caltech, Pasadena, CA, US

Institute for research on exoplanets, Universite 'de Montreal, Montreal, Canada

Received 2019 July 23; revised 2020 January 25; accepted 2020 January 29; published 2020 March 11

Abstract

The gravity field of a giant planet is typically our best window into its interior structure and composition. Through comparison of a model planet's calculated gravitational potential with the observed potential, inferences can be made about interior quantities, including possible composition and the existence of a core. Necessarily, a host of assumptions go into such calculations, making every inference about a giant planet's structure strongly model dependent. In this work, we present a more general picture by setting Saturn's gravity field, as measured during the Cassini Grand Finale, as a likelihood function driving a Markov Chain Monte Carlo exploration of the possible interior density profiles. The result is a posterior distribution of the interior structure that is not tied to assumed composition, thermal state, or material equations of state. Constraints on interior structure derived in this Bayesian framework are necessarily less informative, but are also less biased and more general. These empirical and probabilistic constraints on the density structure are our main data product, which we archive for continued analysis. We find that the outer half of Saturn's radius is relatively well constrained, and we interpret our findings as suggesting a significant metal enrichment, in line with atmospheric abundances from remote sensing. As expected, the inner half of Saturn's radius is less well constrained by gravity, but we generally find solutions that include a significant density enhancement, which can be interpreted as a core, although this core is often lower in density and larger in radial extent than typically found by standard models. This is consistent with a dilute core and/or composition gradients.

Unified Astronomy Thesaurus concepts: Saturn (1426); Planetary interior (1248); Planetary structure (1256); Planet formation (1241)

1. Introduction

1.1. The Gravity Field as a Probe on the Interior

There are a number of fundamental questions that we would like to understand about giant planets. Do they have a heavy-element core? If so, what is its mass? Is it distinct from the overlying H/He envelope, or partially mixed into it? Is the H/He envelope enriched in heavy elements compared to the Sun? Is the envelope fully convective and well mixed?

Unfortunately, the vast mass of a giant planet is completely hidden from view, so that we must use indirect methods to try to answer these questions. Most of our knowledge about the interiors of giant planets comes from interpreting their gravity fields, as recently reviewed for Saturn by Fortney et al. (2018). Because the planets are fluid and rapidly rotating, they assume an oblate shape and their gravitational potential differs from that of a spherically symmetric body of the same mass. The external gravitational potential $V_{\rm e}$ is a function of the colatitude θ and distance r from the center of the planet, and is typically written as an expansion in powers of $R_{\rm eq}/r$, where $R_{\rm eq}$ is the equatorial radius of the planet:

$$V_{\rm e}(r,\,\theta) = -\frac{GM}{r} \left(1 - \sum_{n=1}^{\infty} (R_{\rm eq}/r)^n J_n P_n(\cos\theta) \right). \tag{1}$$

In Equation (1), P_n are Legendre polynomials of degree n. The coefficients J_n ("the Js") are measurable for many solar system bodies by fitting a multiparameter orbit model to Doppler

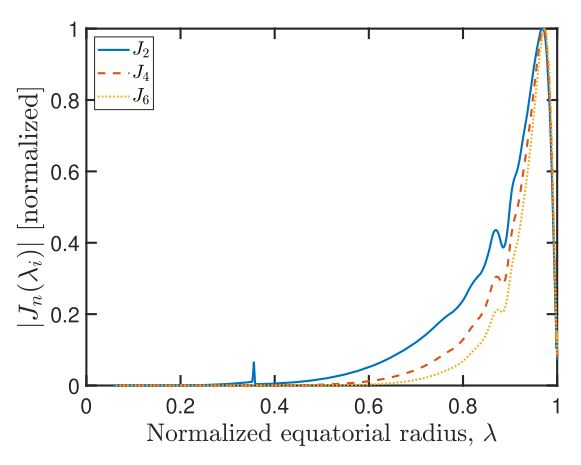
residuals of spacecraft on close approach. For fluid planets in hydrostatic equilibrium, where azimuthal and north-south symmetry hold, only even-degree coefficients are nonzero.

When an interior model for a planet is created, the J_n values are calculated as integrals of the interior density over the planetary volume:

$$MR_{\rm eq}^{\,n}J_n = -\int \rho(\mathbf{r}')(r')^n P_n(\cos\theta')d\tau'. \tag{2}$$

These model J_n can then be compared to measured ones. As is well known, the different J_s sample the density at different depths (with J_2 probing deepest) but with significant overlap, and with most of the weighting over the planet's outer half in radius. This point is illustrated in Figure 1.

The gravity field is a nonunique feature of the interior mass distribution. In other words, different mass distributions can lead to identical gravity signals. This complicates the process of making inferences about the interior structure based only on the external gravity field. In principle, one should explore a wide range of possible interior structures, of possible $\rho(r')$ in Equation (2), to see the full range of solutions that fit the gravity field. Initially, researchers had focused on finding a single, best-fit solution subject to a host of assumptions, chosen for computational convenience and not necessarily following reality. More recently, there have been efforts to explore an expanded range of interior structures, usually by making alternative assumptions about the prototypical planet.



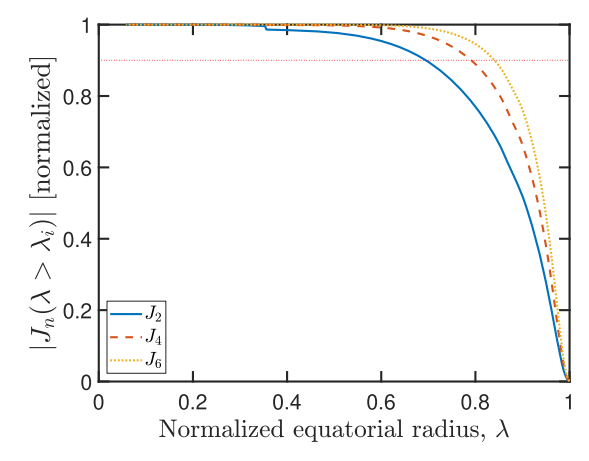


Figure 1. Contribution functions of the gravitational harmonics J_2 (blue solid), J_4 (red dashed), and J_6 (yellow dotted) for a typical, three-layer Saturn model. The contribution "density" $(\propto J(r)dr)$ is plotted in the left panel and the cumulative contribution in the right panel. The horizontal line intersects the curves at a depth where the corresponding J reaches 90% of its final value.

The main contribution of the present work is the introduction of a different approach to the task of inferring interior structure from gravity and the application of this approach to Saturn. The result is a suite of interior structure models of Saturn computed with fewer assumptions and therefore showing a fuller range of structures consistent with observation. We describe our method in detail and compare it with previous work of similar spirit in Sections 1.2.4 and 2.6.

1.2. Common Assumptions in Planetary Interior Models

There are typically at least three significant assumptions or choices that modelers make when constructing interior models of giant planets, thereby implicitly constraining the possible inferences from these models.

1.2.1. The Planets Have Three Layers

Perhaps the most constraining assumption is the prototypical picture of three layers, each well mixed enough to be considered homogeneous. For Jupiter and Saturn, these are a helium-poor outer envelope, a helium-rich inner envelope, and a heavy-element, usually constant-density core. Investigators also adjust the abundance of heavy elements in the He-rich and He-poor layers, with little physical motivation other than it seems to facilitate finding an acceptable match to the gravity field.

While a core–envelope structure is certainly a plausible one, and indeed rooted in well-studied planet formation theories, the assumption of compositionally homogeneous layers may well be a significantly limiting oversimplification.

1.2.2. The Interior Pressure–Temperature Profile Is Isentropic

A typical assumption of interior modeling is that the pressure–temperature profile is isentropic, lying on a single (P, T) adiabat that is continued from a measured or inferred temperature at 1 bar. This second assumption is likely to be true over some of the interior, but there are good reasons to doubt that this holds throughout the interior.

Jupiter and Saturn have an atmospheric He depletion compared to the Sun, and it has long been suggested that this is due to He phase separation from liquid metallic hydrogen in the deep interiors (Stevenson & Salpeter 1977; Fortney & Hubbard 2003). There is likely a region with a He abundance gradient starting between 1 and 2 Mbar in both planets

(Nettelmann et al. 2015; Mankovich et al. 2016). In models that attempt to interpret the gravity field, if such a layer is included at all, it is by interpolation between the outer and inner homogeneous layers (e.g., Wahl et al. 2017; Militzer et al. 2019), but this interpolation is unlikely to capture fully the effects of composition gradients. Composition gradients can inhibit large-scale convection (Ledoux 1947), implying that heat is transported via layered convection or radiation/conduction. This leads to higher internal temperatures that in return allow higher heavy-element enrichment at a given density-pressure. Indeed, nonadiabatic structures have been recently suggested for all outer planets in the solar system (e.g., Leconte & Chabrier 2012; Vazan et al. 2016; Podolak et al. 2019).

1.2.3. The Inferred Composition Relies on Equation of State Calculations

As the field progresses, the equations of state (EOSs) used for modeling giant planet interiors become a better representation of reality. Nevertheless, the EOSs for all relevant materials and mixtures are not perfectly known. Simulations from first principles of hydrogen, helium, and their mixtures over the conditions relevant for giant planets have been carried out and partially validated against experimental data (Nettelmann et al. 2008; Militzer & Hubbard 2013). These EOSs for hydrogen show good agreement with data up to \sim 1.5 Mbar (e.g., Militzer et al. 2016). However, the pressure at the bottom of Saturn's H/He envelope is about 10 Mbar and for Jupiter it is about 40 Mbar, well beyond the realm of experiment. Recent structure models used EOSs for hydrogen and helium based on density functional theory (DFT) simulations (Nettelmann et al. 2008; Miguel et al. 2016; Militzer et al. 2016). Until recently, different EOSs led to different inferred compositions for Jupiter due to different approaches to calculating the entropy. Today, there is good agreement between state-of-theart EOSs (Nettelmann 2017), but it should be kept in mind that DFT also suffers from approximations (Mazzola et al. 2018), and there remains an uncertainty of \sim 2% in the hydrogen EOS, which increases significantly when it comes to predicting hydrogen-helium demixing (Morales et al. 2009).

The heavy elements must also be represented by an EOS (typically for water or silicates), which introduces another source of uncertainty. Therefore, the range of possible compositions and internal structures from such interior models

cannot be taken to be the true range of allowed values, even if the parameter space of possible EOSs, H/He/Z mixing ratios, and outer/inner envelope transition pressures were thoroughly explored.

1.2.4. Appreciating the Complexities

The drawbacks of the assumptions discussed above have long been known and the reality that giant planets are surely more complicated than the traditional modeling framework allows for is generally accepted (e.g., Stevenson 1985). More recent investigations are attempting to allow for a more complex structure. Interior composition gradients due to remnants of formation (Leconte & Chabrier 2012; Helled & Stevenson 2017), core dredge-up (Militzer et al. 2016), convective mixing of primordial composition gradients (Vazan et al. 2016, 2018), and He sedimentation (Nettelmann et al. 2015; Mankovich et al. 2016) have been considered and were found to lead to different structures. Additionally, some investigators have begun using what may be referred to as "empirical" models. In this context, an empirical model is one that is focused on the more direct connection between gravity and density (e.g., Helled et al. 2009) or gravity and equilibrium shape (Helled et al. 2015), without invoking the compositional and thermodynamical origin of these structures.

The work we present here is in the spirit of empirical models. We explore systematically, in a Bayesian inference framework, the possible density profiles of Saturn. We limit our assumptions as much as possible, in order to find the widest range of interior structures with their probability distribution based on their gravitational potential matching the observed field.

2. Composition-independent Interior Density Calculation

The premise of removing some assumptions and deriving composition-free interior density profiles (sometimes referred to as empirical models) is simple and in fact has been pursued in previous works (e.g., Marley et al. 1995; Podolak et al. 2000; Helled et al. 2009). (We discuss similarities and differences with these works in Section 2.6 below.) The only information that is needed to calculate a gravity field is the density everywhere inside the planet, $\rho(\mathbf{r})$, and so this is the only quantity we will directly vary. In fact, hydrostatic equilibrium produces level surfaces—closed surfaces of constant density, pressure, and potential—and therefore a one-dimensional description of the mass distribution is sufficient: we can use $\rho(\mathbf{r}) = \rho(s)$, where s is the volumetric mean radius of the unique level surface of density ρ .

All other properties of the planet will be inferences, rather than input parameters. Because there is unavoidable uncertainty associated with the measurement of the gravity field (and also with its theoretical calculation from interior models; see Section 2.4), this means that there must be a continuous distribution of possible density profiles that fit the gravity solution, and we must base our inferences on the entire distribution. In practice, because we can only ever consider a finite number of solutions, this means that we must base our inferences on a random sample from this unknown distribution of allowed solutions.

In this section, we describe the process of obtaining this random sample, as applied to Saturn. For the most part, the same process would apply equally well to the other giant planets. We mention in places modifications that may be

needed if the same method is to be applied to Jupiter, Uranus, or Neptune.

2.1. Overview

Formally, the distribution we are after is the posterior probability $p(\rho|J^*)$, the probability that the planet's interior density follows $\rho = \rho(s)$ given that the gravity coefficients were measured as J^* . This consists of several subtasks. First, we must find a suitable parameterization of $\rho(s)$. This parameterization should be able to represent all the physically reasonable $\rho(s)$ curves without undue loss of generality, but this is not particularly difficult. It is also necessary that the range and behavior of the numeric values of all parameters are such that they can be efficiently sampled, e.g., with a Markov Chain Monte Carlo (MCMC) algorithm. This is easier said than done, and the best parameterization may be different for different planets.

For Saturn, we find that a piecewise-quadratic function of density as a function of normalized radius works best for the bulk of the planet, with a quartic (degree 4) polynomial required to represent the uppermost region (for $P \lesssim 2$ GPa). We describe this parameterization in detail in Section 2.2. Note that this is one place where modifications might be needed before applying the same procedure to Jupiter or the ice giants.

To drive the sampling algorithm, we need a way to evaluate the relative likelihood of two model planets, and we do this by comparing how well they match Saturn's observed mass and gravity field. The details of this calculation are given in Section 2.3.

The likelihood calculation requires that we know the equilibrium shape and gravity field of a given density profile to sufficient accuracy. Note that in Equation (2) the integrand is known but the integration bounds are unknown. We need to first determine the planet's equilibrium shape. The shape is determined by a balance between the centrifugal acceleration of the rotating planet and the gravitational acceleration. This is therefore a circular problem, requiring an iterative calculation to converge to a self-consistent solution.

We use an implementation of fourth-order Theory of Figures (ToF) using the coefficients given in Nettelmann (2017) and employ optimization techniques that allow us to solve the hydrostatic equilibrium state to desired precision very quickly. The details are given below in the Section 2.4.

The emphasis on speed is necessary, as the next subtask is to employ a suitable MCMC algorithm to draw a large sample of possible ρ . There is no generally agreed-upon method of predicting the number of sampling steps required for convergence. By experimentation, we find that our Saturn parameterization requires tens of thousands of steps to become independent of its seed state and has a long autocorrelation time, requiring a large number of steps following convergence to obtain the desired effective sample size. Producing a valid sample required the computation of about 10 million model planets in total. We give the details of our sampling method and convergence tests in Section 2.5 and Appendix C.

The last step is calculating some derived physical quantities of interest, based on the obtained ρ sample. Given the gravity field, the pressure on each level surface can be computed from the hydrostatic equilibrium equation. And with knowledge of the pressure and density at each level, we may begin to estimate

⁶ Or even of being sure that convergence was reached.

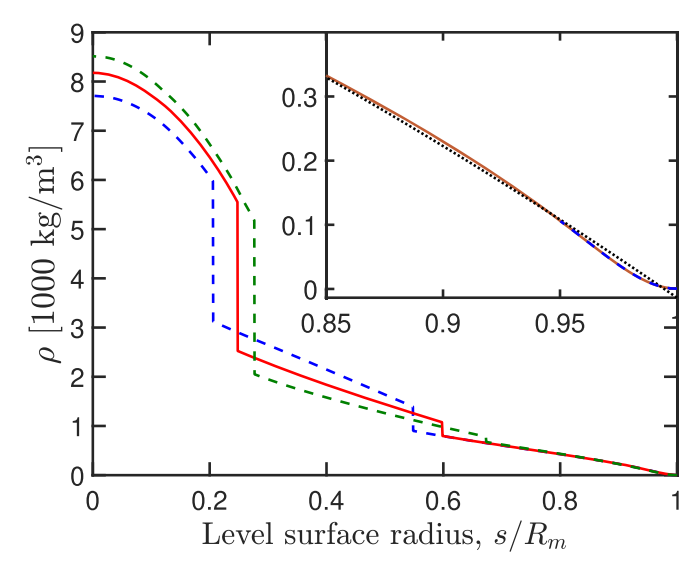


Figure 2. Three representative Saturn density profiles from M19. These profiles were derived using the standard, three-layer assumption, and thus represent only a subset of possible profiles. On the other hand, they are known to be in strict agreement (by construction) with theoretical EOSs throughout the interior. The inset shows a zoomed-in view of the top part of the envelope. The red solid line is the same curve as in the full-scale figure; the black dotted line is a quadratic fit, a good approximation of the upper envelope overall, and the blue dashed line is a quartic fit to the segment $s/R_{\rm m} > 0.94$, a much better fit there (Appendix A).

other quantities of interest, e.g., the helium fraction, the heavyelement content, etc. These quantities are not determined directly by the gravity field but can be inferred, with additional assumptions. We discuss the results of this analysis, as applied to Saturn, in Section 3.

2.2. Parameterization of $\rho(s)$

Our goal is to sample from a space of $\rho(s)$ curves that is as general as possible, making a minimum of assumptions about $\rho(s)$ while still restricting the sample to physically meaningful density profiles and, importantly, keeping the number of free parameters small, for sampling efficiency. These competing requirements are not easy to satisfy, and it may be that the best parameterization depends on the planet being studied as well as on the available sampling algorithms and computing resources.

When looking for a good parameterization of $\rho(s)$, we were guided by previously published work on Saturn's interior. Traditionally derived models are less general than we would like, but they are physically sound. Examining them exposes the major features expected of a $\rho(s)$ curve representing Saturn's interior. Figure 2 shows the density profiles of several Saturn models recently published by Mankovich et al. (2019, hereafter M19). These models assume a three-layer structure for Saturn along the lines of what was considered by Nettelmann et al. (2013). They consist of a homogeneous outer envelope with helium mass fraction $Y = Y_1$ and water mass fraction $Z = Z_1$, a homogeneous inner envelope with $Y = Y_2$ and $Z = Z_2$, and finally a central core with Z = 1. These models assume an additive-volume mixture of hydrogen, helium, and water as described by the Saumon et al. (1995) and French et al. (2009) EOSs, and are assumed to have adiabatic temperature profiles throughout the envelope with an isothermal core.

The general feature is a monotonic and piecewise-smooth function in three segments. This is not surprising, as these models were all derived with the assumption of three layers of homogeneous composition, commonly thought of as an upper envelope, lower envelope, and core. While we do not wish to make such a strong assumption, we find it necessary to make the much weaker assumption that $\rho(s)$ is a monotonic, piecewise-smooth function, with no more than (but possibly fewer than!) two density discontinuities. Further, between discontinuities, the density appears to follow very smooth curves, suggesting that it may be well approximated by a quadratic function of s/R_m for each segment, where $R_{\rm m}=58,\,232\,{\rm km}$ is Saturn's volumetric mean 1 bar radius (Lindal et al. 1985). By experimentation, we find no advantage in using higher-order polynomials to approximate any of the main segments.

This piecewise-continuous model should not be confused with the traditional three-layer one. The assumption of density being piecewise continuous is much less strict than that of composition being piecewise constant, even if they lead to visually similar plots. Nevertheless, it would be even better to allow more discontinuities or, better yet, a variable number of them. While this may seem like a relatively straightforward generalization, it would in fact greatly increase the computational cost of sampling the parameter space. To understand why, consider that each additional discontinuity in $\rho(s)$ not only introduces four additional parameters (the three parameters required to describe the quadratic plus the location of the additional break point), these parameters will also be highly correlated with the rest. As it turns out, this correlation is already evident with just two discontinuities. Informally, each of the two density "jumps" can substitute for the other in the large subset of models where only a single pronounced discontinuity appears. This evident "redundancy" is by no means proof that there cannot be more than two sharp density jumps in Saturn's interior. But it helps us accept, at least temporarily, a compromise between maximum generality and minimum CPU hours.

When we examine more closely the very top of the density curves in Figure 2 we find that the uppermost part of the envelope (by radius, $r \gtrsim r_a = 0.94 R_{\rm m}$) does not follow the same quadratic as the rest of the upper envelope. Instead, it is more similar to a quartic polynomial. This is demonstrated visually for one density profile in the inset of Figure 2 and in more detail in Appendix A. In this low-pressure region, the physical models are based on well-tested EOSs of H and He, and the assumption of an adiabatic gradient is appropriate, so we would be well advised to constrain our profiles to make use of this information. In Appendix A we explain how we derive a one-parameter family of quartic functions that keeps us grounded to realistic density values in the region above r_a , while still allowing variation by letting the value of $\rho_a = \rho(s = r_a)$ be sampled.

It is important to note that to date, all EOS-based models of Saturn find solutions consistent with the measured gravity field that predict a concentration of heavy elements in the envelope of at most a few times the protosolar value (e.g., Helled & Guillot 2013; Nettelmann et al. 2013; Militzer et al. 2019), while Saturn's atmospheric spectra indicate a higher value, perhaps as high as 10 times the protosolar metallicity (Atreya et al. 2016). In principle, atmospheric enrichment might not represent the bulk composition of the outer envelope, as was

recently suggested for Jupiter (Debras & Chabrier 2019). Nevertheless, this demonstrates that, while we wish to be guided by physical models, our parameterization must not be overly constrained by them.

To summarize, we arrive at the following parameterization, using $z = s/R_m$:

$$\rho(z) = \begin{cases} \rho(z, [\mathbf{q}_1, \mathbf{q}_2, \mathbf{q}_3, z_1, z_2]), & 0 < z < z_a \\ \rho(z, [\mathbf{Q}(\rho_a)]), & z_a < z < 1. \end{cases}$$
(3)

Here, q_1 are the three parameters defining the first (outermost) quadratic segment, q_2 are the three parameters defining the second (middle) quadratic segment, and q_3 are the three parameters defining the third (deepest) quadratic segment. There is more than one way to let three numbers define a quadratic, and although they are all equivalent, the associated range of values and degree of correlation make some choices better suited for MCMC sampling. The precise definition of q_i that we find, by trial and error, to work well in this case is given in Appendix B. The transition between the first and second segments is at normalized radius z_1 (which we let vary from 0.35 to 0.9 in normalized radius), and the transition between the second and third segments is at $z_2 < z_1$ (which we let vary from 0.1 to 0.4). The top of the upper envelope is defined by the quartic polynomial $Q(\rho_a)$ for $z > z_a = 0.94$. The values in Qand their definition are given in Appendix A. The quartic segments are uniquely determined by the density at z_a , itself already determined by the coefficients q_1 . We thus have 11 free parameters—three each for the three quadratic segments, plus the two "floating" transition radii.

2.3. Comparing Model and Observation

MCMC sampling works by comparing, at every iteration, the likelihood of a proposed vector of parameter values, L(y), with that of the current vector of parameter values, L(x), and accepting or rejecting the proposed values with probability proportional to the relative likelihoods. If the likelihood function is itself proportional to the desired (unknown) posterior probability, in our notation, if $L(x) \propto p(\rho(x)|\text{OBS})$, then the resulting Markov chain will converge, in the long run, to a sample from that posterior. For OBS, we substitute any number of observed quantities that may differ from those calculated in the model.

A likelihood function that is proportional to the desired posterior is the function $L(x) = p(OBS|\rho(x)p(x))$. It is proportional to the posterior as a consequence of Bayes' rule. The prior probability p(x) is necessary. It is our informed, subjective assessment of what values the model parameters x are expected to take, and typically, it is a simple product of the individual prior probabilities of the independent variables x_i , which in turn are either uniform or normal inside a region of reasonable values. What we need then is to provide the MCMC algorithm with a function that evaluates the relative goodness of the match between the observed properties of the planet and the values of the same properties as calculated for the model, taking uncertainties from both model and observation into account.

In this context, the planetary properties that our models need to match are the gravity coefficients J^* and the planet's mass M_{Sat} .

First, the gravity. We assume that the observed values J^* are normally distributed about the true, unknown, mean values and

calculate a distance:

$$D_J^2 = \left(\frac{J_2 - J_2^{\star}}{\sigma_{J_2}}\right)^2 + \left(\frac{J_4 - J_4^{\star}}{\sigma_{J_4}}\right)^2 + \left(\frac{J_6 - J_6^{\star}}{\sigma_{J_6}}\right)^2, \tag{4}$$

where the σ_{J_i} are measures of the uncertainty in either the measured or the computed values, or both.⁸

In the work presented here, only J_2 , J_4 , and J_6 were considered for the purpose of calculating the likelihood function. Higher-order coefficients J_8 – J_{12} , as well as nonvanishing oddindexed coefficients J_3 and J_5 , have been measured for Saturn, to impressive precision, by the Cassini Grand Finale gravity experiment (Iess et al. 2019). But it seems clear that these reflect an increasingly large contribution from an asymmetric and/or time-varying field, deriving either from planet-scale differential rotation or from deeply rooted zonal winds, or both (Galanti & Kaspi 2017; Kaspi et al. 2018; Galanti et al. 2019; Iess et al. 2019). These phenomena are important in themselves and offer a promising avenue for studying further Saturn's dynamic nature, but for the purpose of constraining the bulk interior structure, their net result is to increase the effective uncertainty of the loworder Js ascribed to solid-body rotation (Guillot et al. 2018). Studies of differential rotation on Saturn demonstrate that their contribution to the low-order even harmonics can be significant (Hubbard 1982; Galanti & Kaspi 2017). As our goal is to capture the widest range of probable interior structures, we compute Equation (4) for every model by assuming solid-body rotation and setting $J_2^{\star} = 16290.573 \times 10^{-6}$, $J_4^{\star} = -935.314 \times 10^{-6}$, and $J_6^{\star} = 86.340 \times 10^{-6}$ (Iess et al. 2019), with uncertainties $\sigma_{J_2} = 1.5 \times 10^{-5}$ and $\sigma_{J_4} = \sigma_{J_6} = 5 \times 10^{-6}$. The values adopted for the uncertainties come from interpreting the largest contribution from winds found in Galanti & Kaspi (2017), their Figure 4, as a symmetric, two-sigma range.

We cannot simultaneously hold fixed both the total planetary mass and the surface radius while also specifying the density at all radii. As we use the density ρ_a as one of the sampled parameters, the converged hydrostatic interior profiles can be scaled to fix $R_{\rm eq}$ or M precisely, but not both. Saturn's mass and radius are known to comparable precision, and it is convenient to fix all models to $R_{\rm eq}=60$, 268 km, Saturn's measured equatorial radius at the 1 bar level (Lindal et al. 1985). The calculated mass of a converged and scaled density profile will therefore exhibit a small spread around a nominal value, leading to another distance term:

$$D_M^2 = \left(\frac{M - M_{\text{Sat}}}{\sigma_M}\right)^2,\tag{5}$$

with $M_{\rm Sat} = 568.336 \times 10^{24} \, \rm kg$ and $\sigma_M = 0.026 \times 10^{24} \, \rm kg$ (Jacobson et al. 2006, https://ssd.jpl.nasa.gov). Then, assuming that σ_M and σ_J are uncorrelated, we use $D^2 = D_J^2 + D_M^2$ as a measure of a model's fit to observation and a natural likelihood function is

$$L \propto \exp\left(-\frac{1}{2}D^2\right)p(x). \tag{6}$$

A full definition of our chosen prior is given in Appendix C.

Depending on the source of uncertainties σ_{J_i} , they may be correlated. In that case, the definition of D_J would involve a covariance matrix but the rest of the calculation would remain unchanged.

 $^{^9}$ *GM* is measured with exquisite accuracy, but *G* is known to $\sim 10^{-4}$ precision (CODATA 2014, https://physics.nist.gov).

We need not worry about a normalizing constant as the sampling algorithm evaluates only ratios of likelihood.

A final minor modification of Equation (4) is worth mentioning. Because the uncertainty values that define the σ_{J_i} are due in large part to the contribution from nonrigid rotation, and because this contribution, while unknown in detail is very likely to be nonzero, it seems unwarranted to "privilege" the point J^* as the Gaussian likelihood (6) does. Instead, we measure the distance of a model's gravity not to the center, J^* , but to the nearest corner of the cube defined by $J_i^* \pm \sigma_{J_i}$. Models inside this " 1σ cube" are considered equally likely. This likelihood seems to us more physically justified. It turned out to have a negligible effect on the derived samples, however.

2.4. Fast Calculation of Gravity Coefficients

The main computational effort involved in the sampling, and thus the prime candidate for optimization, is the calculation of the gravity coefficients¹⁰ $J = [J_2, J_4, J_6]$ given a particular $\rho(s)$.

The calculation of the J_i for fluid planets has a long and rich history. In modern times, the choice is between two algorithms. The faster but less precise method is the ToF (Zharkov & Trubitsyn 1978). When carried to fourth order in powers of the small parameter $m = \Omega^2 R_m^3/GM$, where Ω is the uniform rotation rate and GM is the total gravitational mass, the theoretical truncation error is $|\delta J_2/J_2| \lesssim 10^{-4}$ and $|\delta J_4/J_4| \lesssim 10^{-3}$. We use the shape-function coefficients given by Nettelmann (2017) to $\mathcal{O}(m^4)$ and confirm her findings that this level of precision is also achievable in practice. For Saturn, the Cassini mission's Grand Finale orbits provided gravity coefficients to much better precision, 11 but as discussed above, the measured values include a potentially large contribution from dynamic flow (winds), greatly increasing the effective uncertainty in the portion of the gravity field attributed to the underlying density structure. For J_2 , the wind contribution becomes the dominant source of uncertainty, while for J_4 and J_6 , the winds and the uncertainties associated in the ToF calculation are comparable in magnitude and are therefore added, in quadrature, to define σ_L .¹²

The solid-body rotation period for Saturn is itself still somewhat uncertain. The rotation period measured long ago by *Voyager* as 10^h39^m24^s (Desch & Kaiser 1981) is now commonly understood to be much too slow to represent the bulk planetary rotation. More recently several estimates of a faster rotation rate have been proposed, based on a few independent methods that seem to point to a period of 10 hr and between 33 and 34 minutes (Read et al. 2009; Helled et al. 2015; Mankovich et al. 2019; Militzer et al. 2019), but an exact rotation rate is not available. The uncertainty in rotation rate can be used to estimate a corresponding correction to the already large gravity uncertainty, but there is a better way.

We can let the rotation parameter m be itself a sampled variable, guided by a suitable prior as always. Adding an extra variable to a sampling problem is a risky proposition, but in this case it turned out to have minimal performance cost, because the rotation parameter is uncorrelated with the other sampled variables and because the likelihood function is not

strongly sensitive to this variable, at least within the range of values implied by the prior. We use a relatively strong prior of normally distributed m centered on $m^* = 0.14224 \ (10^{\rm h}33^{\rm m}30^{\rm s})$ with $\sigma_m = 4.5 \times 10^{-4} \ (\sim 1 \ \rm minute)$.

The second option for calculating the Js is the Concentric Maclaurin Spheroids method (CMS; Hubbard 2012, 2013), which allows for calculation of J_i of any order and to arbitrary precision, but at the cost of a much slower computation. The CMS method was developed in anticipation of the extraordinarily precise data expected from the Cassini Grand Finale orbits (and similarly precise measurements of Jupiter's gravity by *Juno*). However, although the radio science indeed determined Saturn's gravity to very high precision (Iess et al. 2019) as discussed above, the presence of nonuniform rotation leads to effective uncertainty much higher than the measurement uncertainty. The large uncertainty associated with deep zonal winds means that the faster ToF method is adequate for the purpose of calculating the rigid-body Js. In this work, we therefore let ToF do the majority of the calculation, including all of the computation embedded in the sampling process. We use CMS for validation and to compute a subset of some tens of high-likelihood models.

Both CMS and ToF can benefit from the following optimization. To achieve the theoretical level of precision, the integrals involving the mass distribution $\rho(s)$ must be computed with higher accuracy than that required by the rest of the algorithm. In general, this means that $\rho(s)$ must be resolved on a fine-enough grid in normalized radii, z_i , for the numerical integration to properly converge (e.g., Nettelmann 2017, Equation B.9). It is not necessary, however, to carry out the computationally expensive solution of nonlinear equations for the shape functions, in the case of TOF, or the root finding of potential as a function of latitude in the case of CMS, on such a fine grid. Because the shape of the planet deviates only slightly from spherical even for a fast rotator such as Saturn, the shape of a level surface, $r(z, \theta)$, is a very smooth function in both z and colatitude θ . Taken as a function of z for fixed θ , the function can be interpolated with excellent precision from only a handful of known values between z = 0 and z = 1, using a spline interpolant.

This affords us a significant reduction in the time required to compute the shape and gravity for a single model. For example, we find that we can achieve the expected theoretical precision of fourth-order ToF with $\rho(s)$ resolved on N=2048 levels but with the shape equations solved on only n=64 intermediate levels, and then interpolated onto the full set. Our implementation then returns a candidate model's gravity coefficients in under 1 s running on a single CPU core. This is a key optimization that allows the sampling procedure to be completed on modest hardware.

The same optimization can be implemented for CMS with even better results, as demonstrated in Militzer et al. (2019). Unfortunately, for a sampling problem of this scope, this speedup is not enough to mitigate the speed disadvantage of CMS compared with ToF.

2.5. MCMC Sampling of Parameters

There is a wide variety of MCMC sampling algorithms; all fundamentally seek to sample the posterior distribution by a sequence of random steps through parameter space. The main difficulty is constructing an appropriate random-stepping

 $[\]overline{^{10}}$ Higher-order Js can be used when appropriate; the computation time is independent of how many Js are sought.

¹¹ The same would be true for Jupiter, with gravity obtained during the *Juno* mission, whereas for Uranus and Neptune the measurement uncertainty would still be dominant (Hubbard et al. 1995).

¹² The values of σ_{J_i} given in Section 2.3 include both sources.

algorithm, called a proposal distribution, to efficiently explore a high-dimensional parameter space.

MCMC can often benefit from parallel execution. A variant that has proved very useful for this work is the parallel stretchmove algorithm (Goodman & Weare 2010), as implemented in the emcee Python package (Foreman-Mackey et al. 2013). In this algorithm, the proposal distribution is automatically constructed by taking a step along the line segment (in parameter space) connecting the current position of two "walkers" in an ensemble that explores parameter space simultaneously. This greatly simplifies the most difficult task of MCMC but if the walkers in the ensemble are run in serial, the computation time would be too long. Luckily, this approach can benefit from parallelization with minimal overhead and is thus perfectly suitable to run on a large supercomputer. The sampling calculations for this work were run on NASA's Advanced Supercomputing facility at the Ames Research Center.

A critical consideration in the application of any MCMC algorithm is the issue of convergence. Simply put, we must decide when it is safe to stop the sampling run and use the obtained draws to calculate anything of interest, trusting that the sample distribution is similar enough to the underlying posterior. Theoretical considerations offer only loose bounds on the variance of sampled parameters and are rarely useful in practical work. A number of diagnostic schemes that attempt to either hint at convergence or to warn of a failure to converge (e.g., review by Cowles & Carlin 1996) have been suggested. But even this more limited task is still an open problem in statistics, and the decision to accept a sample as "converged" still involves case-by-case, subjective judgment. Appendix C includes a discussion of the mixing and burn-in length of our samples.

In our case, examining the traces, autocorrelations, and joint posteriors of partial samples, we find that we can significantly accelerate convergence by separating our 12 dimensional parameter set into two subsets that are sampled in hierarchical fashion. Recall that of the 11 parameters needed to define a $\rho(s)$ curve (Equation (3)), 2 are the normalized radii locating the points of possible density discontinuity; their values have a straightforward, physical meaning. The other nine parameters, defining the geometry of the quadratic segments, take values whose highly nonlinear effect on the density is entirely dependent on the value of the first two parameters. In statistical terms, we have two proper subsets of parameters with very high correlation between sets but low correlation within each one. Consequently, fixing values for the transition radii, we can sample the conditional joint posterior of the nine geometric parameters efficiently. Of course, we must repeat this sampling many times, on a fine grid of values for the transition radii, and finally combine the conditional probabilities to a full joint posterior. But the gain in sampling efficiency provided by this hierarchical approach is such that we still come out ahead in terms of CPU hours and overall length of simulation. There is more than one way to combine conditional joint probabilities to a single joint posterior. We use the Bayes Information Criterion, defined fully in Appendix C.

A final minor optimization is worth mentioning. In hydrostatic equilibrium, the condition $dP/dr = -\rho g$ requires that the pressure gradient go to zero at the center of the planet. For a continuous thermal profile, this implies that the density

gradient likewise vanishes at the center, in our notation:

$$\lim_{s \to 0^+} \frac{d\rho(s)}{ds} = 0. \tag{7}$$

Because $\rho(s)$ is in our case piecewise quadratic, the linear term of the innermost quadratic segment should vanish, or equivalently, that any three parameters used to define the quadratic are correlated, such that only two independent parameters are needed. This not only results in more realistic density profiles but also helps by reducing the dimensionality of the sample space—always a good idea.

2.6. Relation to Previous Works

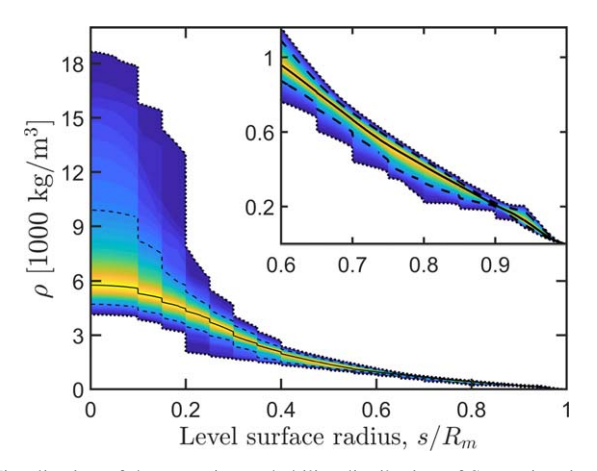
While in previous sections we discussed the drawback of "standard" approaches, here it is worth discussing how our work compares to previously published alternative approaches.

Helled et al. (2009, 2011a) investigated models for Saturn, Uranus, and Neptune where the interior $\rho(s)$ profile was parameterized as a high-order polynomial. A single best-fit polynomial was found, given the gravity field, and the results were interpreted by comparison with physical EOSs for H, He, ices, and rock. In other studies, a large range of density profiles was considered, allowing for different core masses and radii, with the core being represented by a constant density (Helled 2011; Helled et al. 2011b; Kaspi et al. 2013). Our work has a similar spirit but we determine the statistical distribution of the empirical models while also allowing a more general structure, and more than one density discontinuity, which is favored by the gravity solution.

Another approach was that of Leconte & Chabrier (2012), who investigated Jupiter and Saturn structure models that were super-adiabatic throughout most of the interior, due to an ad hoc composition gradient in the planetary interior. These models yield significantly different interior structures (that were much richer in heavy elements than standard models), but there was little exploration of a range of models. Vazan et al. (2016, 2018) ran evolution models of Jupiter and Saturn with composition gradients and helium settling for Saturn, and several models have been presented, not aimed at a statistical description.

Another approach to interior modeling that is quite similar to ours in spirit but very different in practice was previously attempted by Marley et al. (1995) and Podolak et al. (2000). As a means to forgo as many assumptions as possible, the authors studied a number of randomly generated interior density profiles for Uranus and Neptune, matching only the constraints of mass, radius, J_2 , and J_4 . Their model generation was truly random, not based on a sampling algorithm. Naturally, this algorithm, while simple, has a very low success rate, i.e., the number of valid models per n models generated was quite low, and the authors were forced to restrict the parameter space in some arbitrary ways, the most important was forcing a single value for the core radius and a small range of radii for a secondary density jump in the envelope.

Even with these restrictions, the investigation was able to produce only a small number of valid models for each planet, much too small to draw statistical conclusions from, particularly as this set of empirical density curves was not constructed to be a representative sample. Nevertheless, the models thus obtained were different from models generated by the traditional approach in interesting ways. Most importantly,



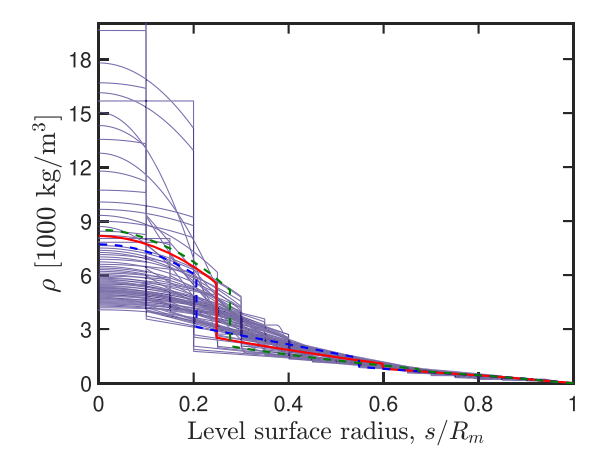


Figure 3. Visualization of the posterior probability distribution of Saturn interior density profiles. Left: the thick black line is the sample median of density on each level surface. The dashed lines mark the 16th and 84th percentiles, and the dotted lines mark the 2nd and 98th percentiles; between the lines, the percentile value is indicated by color. Right: several hundred profiles covering the sampled range. By nature of the MCMC algorithm, regions of the figure where lines are closer together correspond to high-likelihood areas of parameter space. For comparison, three profiles derived by physical models with a pure H_2O core (Mankovich et al. 2019, same profiles as in Figure 2) are overlaid.

the derived pressure—density relation for both Uranus and Neptune implied a gradual composition gradient in the outer shells of both planets (Marley et al. 1995, their Figure 2).

3. Saturn's Density Profile and Inferred Properties

After obtaining an independent random sample from the posterior in parameter space, we examine the resulting distribution of density profiles. Figure 3 is a view of the sample distribution. Density is plotted against the normalized level-surface radius. In the left panel, the thick black curve is the ensemble median density at each radius, and the shaded regions indicate the width of the distribution. In the right panel, a subset of the entire sample is plotted, selected to illustrate the sample range. Regions of higher line density (where the lines are closer together) correspond to high-likelihood areas in parameter space, by the nature of the MCMC algorithm. The EOS-based profiles from Figure 2 (from M19) are overlaid for comparison.

Two insights are possible by inspection of Figure 3. First, from the left panel, the observed gravity can constrain the top half of the planet much more strongly than it can the bottom half. This was expected (see Figure 1), but it is worth emphasizing again that it is a fundamental limitation of using gravity to probe the interior. This limitation is with us to stay; it will not be completely removed by increasing the accuracy of measurement or the precision of calculations. The same point is illustrated quantitatively in Figure 4 where the sample-spread of density values is shown for each radius. The variation in density also translates to a spread in moment of inertia values, which end up approximately normally distributed, with a mean of 0.2219 and standard deviation 0.0005.

The second interesting feature, easier to spot in the right panel, is the existence of density discontinuities. Recall that our parameterization allowed up to two discontinuities; it did not require any. Indeed, many profiles in the ensemble lack one or both discontinuities, the interpretation being that they lack a sharp composition or phase boundary.

The inner discontinuity, at $s = s_2$, was meant to represent the possibility of a distinct core. Many density profiles indeed show a discontinuity pronounced enough to clearly indicate a transition to a heavy-element core, while in many others, a much smaller density jump is observed instead, indicating a

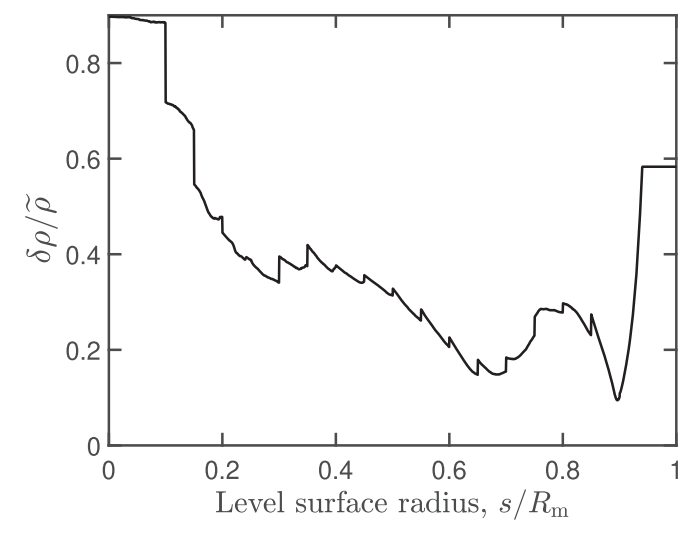


Figure 4. Width of the distribution of density values found in the posterior sample at each radius. The quantity $\delta\rho$ is the difference of 84th and 16th percentile values, giving the equivalent of a 2σ spread; $\tilde{\rho}$ is the sample median density. The flat region near $s/R_m=1$ is a consequence of the relatively strong prior imposed in that region (see Appendix C).

more subtle composition change, consistent perhaps with the idea of a fuzzy/dilute core (Helled & Stevenson 2017) or compositional gradients (Leconte & Chabrier 2012; Fuller 2014). For illustration, subsets from the sample with and without a pronounced discontinuity are shown in Figure 5 (left panel). To put a probability value on the existence of a heavyelement core, we can look at the distribution of $\Delta \rho/\rho$ at $s = s_2$, shown in Figure 6, but it is not clear what "cutoff" value should indicate the core/no-core property. For reference, we can look at previously published, EOS-based models where a core was explicitly assumed. In such models, the relative density jump at the core boundary exhibits a wide range, from as low as $\Delta \rho / \rho \approx 0.3$ to more than tripling the density (e.g. Vazan et al. 2016; Mankovich et al. 2019). With this in mind perhaps the most precise statement to make is that at least half the density profiles in our sample show a discontinuity pronounced enough to be consistent with a heavy-element core transition.

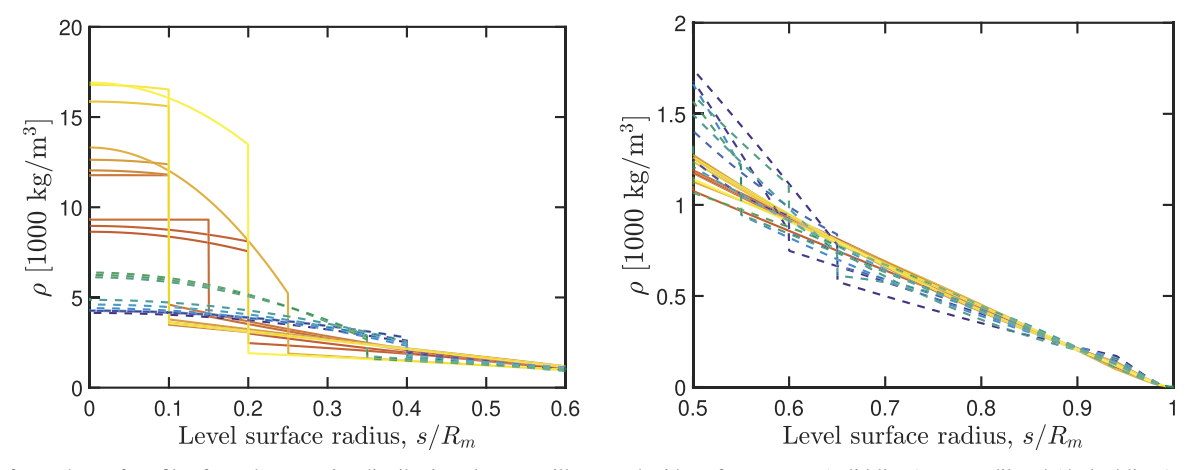


Figure 5. Left: a subset of profiles from the posterior distribution chosen to illustrate the idea of a compact (solid lines) versus diluted (dashed lines) core. All have comparable likelihood values. A precise value of $\Delta\rho/\rho$ marking the difference between compact and diluted cores is hard to define (see discussion in the text). Right: a subset of profiles from the posterior distribution chosen to illustrate the possibility of continuous He abundance in the envelope (solid lines) as well as the traditional idea of helium rain separating He-poor and He-rich layers (dashed lines). Again, the likelihood values of both subsets are comparable and, again, a precise cutoff below which the curve is considered continuous is not obvious.

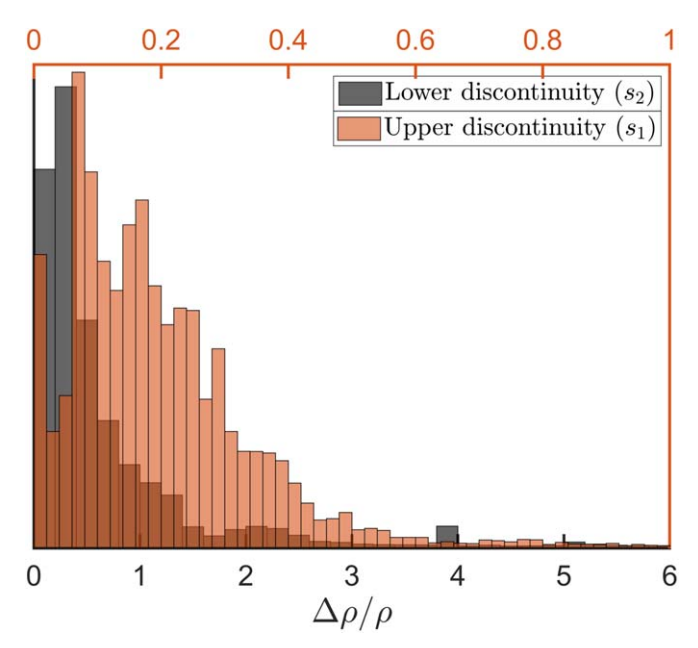


Figure 6. Histograms of the density increase at the inner (bottom axis) and outer (top axis) discontinuities, perhaps representing a phase or composition change.

The outer discontinuity, at $s = s_1$, was meant to represent the possibility of an abrupt change in density in the envelope, where the He mass fraction changes from depleted (relative to protosolar values) to enriched. This transition was expected based on theoretical considerations about the miscibility of He in H, in the region of phase space where hydrogen undergoes a molecular-to-metallic phase transition (Stevenson 1975). An abrupt change in He mass fraction, Y, is often explicitly included in interior models, usually as a free parameter. However, this two-layered envelope is only one possible arrangement among many, including a continuous Y gradient. For example, if Saturn's interior is sufficiently cold for He phase separation to occur in the first place, then it is true that helium distribution is determined by the precise solubility of helium throughout the metallic interior, quantitative predictions of which have been made from first-principles simulations (Schöttler & Redmer 2018). Applying these predictions self-

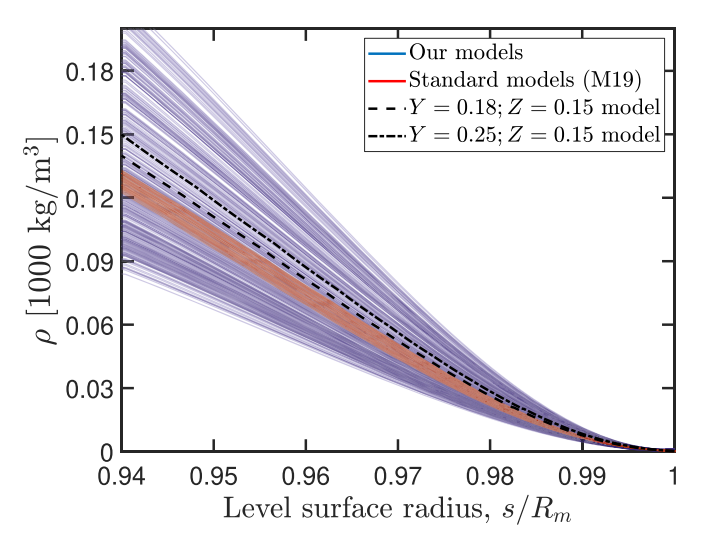
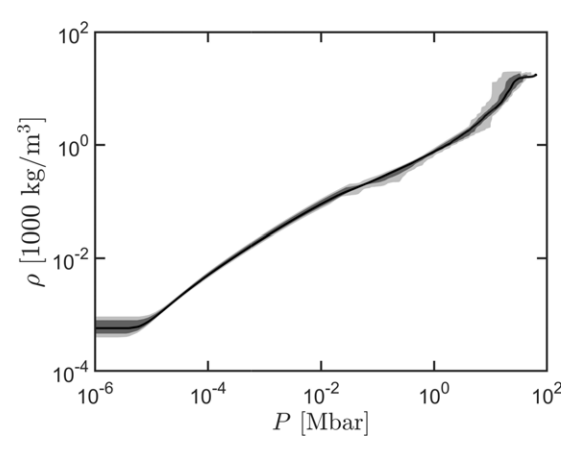


Figure 7. Density profiles in the upper envelope derived from our composition-agnostic sample (purple), traditional three-layer models with standard values of $Z \lesssim 0.05$ (M19, red), and two three-layer models that have a much higher value of Z=0.15 consistent with atmospheric abundances (black dashed and dotted–dashed) but do not fit the observed gravity field.

consistently to Saturn interior models, Mankovich & Fortney (2019) find equilibrium profiles wherein helium abundance increases continuously with depth inside $P \approx 2$ Mbar with the exception of a single deep discontinuous jump in density connecting the helium gradient region with a deeper pool of undissolved helium-rich material.

The sampled profiles include both continuous-density envelopes as well as those with small density jumps at s_1 . While a density jump does not uniquely correspond to a jump in He abundance, a continuous $\rho(s)$ does imply continuous Y(s). As seen in Figure 6, both possibilities (illustrated in the right panel of Figure 5) are consistent with the observed gravity.

Perhaps the most useful aspect of the empirical-model approach is the possibility of finding unexpected solutions that can never arise where explicit composition modeling is used. Figure 7 takes a closer look at the density solutions, this time focusing on the low-pressure region above ~ 2 GPa. A long-standing point of tension in Saturn modeling is that Saturn's



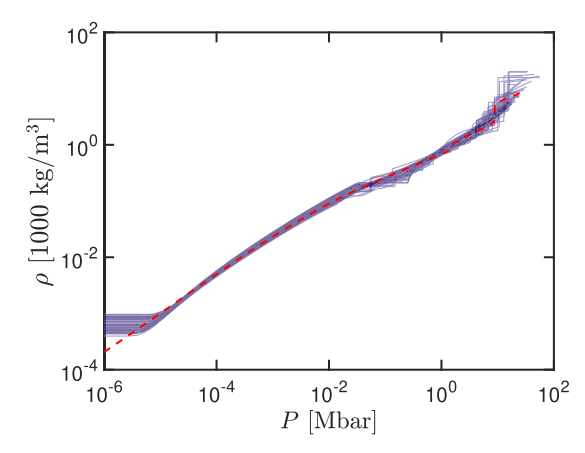


Figure 8. Visualization of the posterior distribution of empirical Saturn barotropes (pressure–density relations). Left: the sample median (thick black line), 16th to 84th percentile range (dark gray shaded), and 2nd to 98th percentile range (light-gray shaded). Right: thinned subset of sampled barotropes. The median barotrope implied by the physical models of M19 (red dashed line) overlaid for comparison.

atmosphere is known to be enriched in heavy elements (Atreya et al. 2016), showing about 10 times the solar abundance for C, P, and S (seen in CH₄, PH₃, and H₂S). That is, a "metals" mass fraction of $Z \approx 0.15$ for the H/He envelope. However, modern Saturn models, even after the Grand Finale orbits, find a fit to the gravity field only with a much lower Z < 0.05 in the outer H/He envelope (Nettelmann et al. 2013; Iess et al. 2019; Mankovich et al. 2019). Traditional models cannot match all of the atmospheric constraints, suggesting that we do not have a complete picture of Saturn's interior. In contrast, we find that a natural outcome of our composition-agnostic approach is density-enhanced outer layers. For comparison, we show two traditionally calculated models with Z = 0.15 in their envelopes, and they fall nicely inside our posterior sample. The density profiles in our sample (purple lines in Figure 7) fit the measured gravity field while the traditional model cannot, with such high Z fraction, because of quite different deeper interior profiles (Figure 3).

3.1. Inferences on Possible Composition

With each $\rho(s)$ profile is associated a corresponding pressure profile, P(s), by assuming hydrostatic equilibrium. Combining the two profiles to eliminate the radius variable results in a unique pressure–density relation, often called a barotrope. The posterior distribution of Saturn barotropes implied by our sample is shown in Figure 8. By itself, the barotrope distribution does not provide much new insight; however, it serves as the basis for the derivation of implied constraints on composition, by comparison with known EOSs, described next.

So far we have focused our attention on what the gravity implies directly about the interior, avoiding additional assumptions. We now wish to see what can be inferred about the planet's composition; some assumptions and approximations become necessary. The reason is that the density and pressure are not determined solely by composition; the thermal structure is a separate, and unknown, variable. Although the 1 bar temperature (to be used as a boundary condition) can be determined by observation, the interior thermal profile is unknown unless we make the strong and not entirely justified assumption of a single adiabatic profile extending at least some fraction of the way down into the planet (Section 1.2).

A possible approach is to compare the empirical barotropes obtained above to some reference barotrope and examine the "residual" density for possible constraints on composition. Deviations of the density in the sampled profiles from this reference are due to a combination of the actual composition being different from the assumed reference and of the real temperature profile being different from adiabatic. ¹³ This degeneracy means that we can only hope to estimate bounds on composition, rather than a nominal value.

In detail, the calculation is this: given the density ρ and pressure P on a level surface with mean radius s, we can compute $\rho_{\rm bg} = \rho_{\rm bg}(P)$ using a background (bg) EOS and an assumed thermal gradient to compute a background barotrope. The residual density, $\rho - \rho_{\rm bg}$, is already instructive, but we can further compute $\rho_{\rm fg} = \rho_{\rm fg}(P)$ using a foreground (fg) barotrope for heavy elements (water or rock) with the same pressure and temperature as the background. The heavy-element mass fraction Z then follows from the additive-volume formula,

$$\frac{1}{\rho} = \frac{1 - Z}{\rho_{\text{bg}}} + \frac{Z}{\rho_{\text{fg}}}.$$
 (8)

The mass fraction Z, calculated with different choices for the foreground EOS, can be used to constrain the heavy-element content consistent with the sampled density profiles.

In the simplest case, our background can be a mixture of only hydrogen and helium in protosolar mass fraction with an adiabatic temperature gradient. We use the EOS of Saumon et al. (1995) to generate pressure–density points for H (X=0.725 by mass) and He (Y=0.275 by mass) with constant entropy corresponding to a temperature T=140 K at a pressure of P=1 bar. The residual density of the sampled profiles relative to this background is shown in Figure 9. Clearly, there is an excess density compared to the adiabat in the regions of the planet below 70% of the planet's radius, which becomes extreme in the inner 30%. If a lower Y reference adiabat were chosen in the outer layers, larger density excess would be needed.

Next, using a foreground EOS for either pure water ice (Thompson 1990; French et al. 2009) or pure rock (Thompson 1990), we apply Equation (8) to each of the sampled profiles. What we obtain is an empirical probability distribution of the heavy-element content in Saturn's interior. In Figure 10, we

¹³ And if the reference barotrope was constructed using a theoretical equation of state, then of course there is an additional source for the deviation—the accuracy of the underlying EOS.

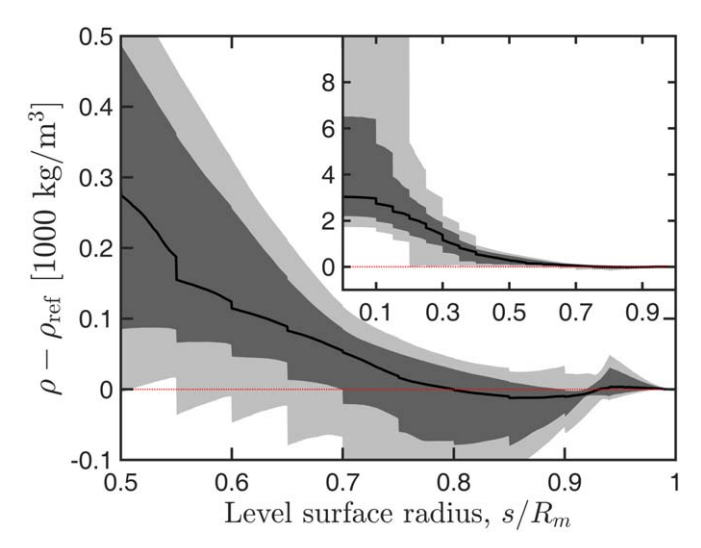


Figure 9. Residual density above a background derived from a reference adiabat calculated for a H/He mixture with He mass fraction Z=0.275 and T(1 bar)=140 K. The thick curve is the sample median, and the dark and light shaded regions include 68% and 96% of the sample, respectively.

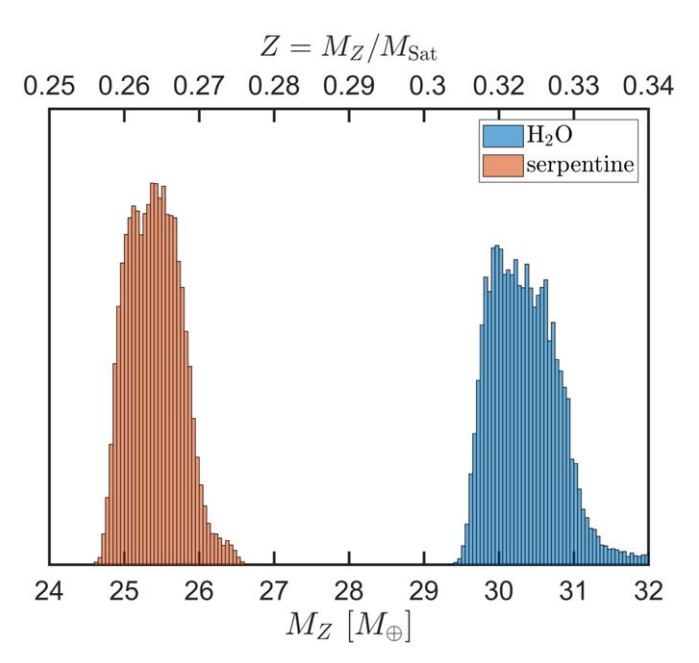


Figure 10. Residual mass in heavy elements and corresponding residual bulk metallicity assuming either pure H_2O ice or pure serpentine rock EOS. These are end-members of what is likely a mixture of both materials in unknown ratio. The figure shows the mass in heavy elements inferred with a reference density based on a H/He adiabat with Z=0.275 extending throughout the planet. It should be interpreted as an upper bound for adiabatic models, as it excludes the possibility of a pure heavy-element core.

plot a histogram of this distribution, which should be taken as an estimated upper bound rather than a precise distribution, given the assumptions underlying this calculation. These values are typically higher than those from standard models because the excess heavy elements, even at high pressure where one might expect a pure heavy-element core, are here always determined as an excess density over that of the lower density H/He.

The same calculation can be repeated for different internal thermal structures or with different choices of background and foreground EOS. There is no need to repeat the time-

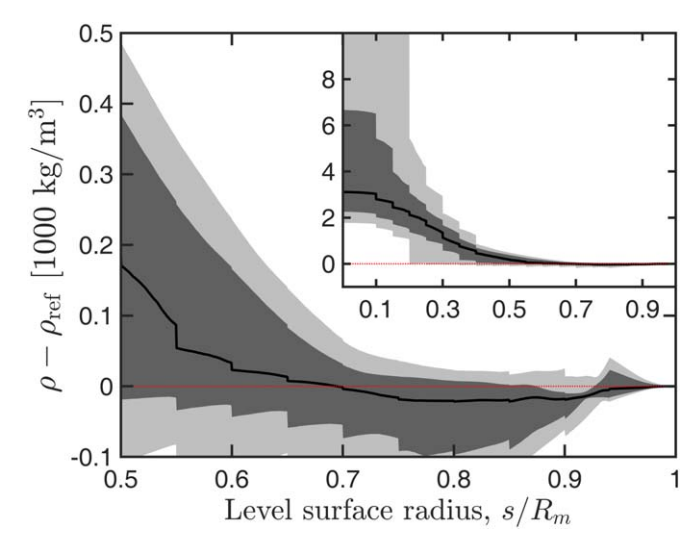


Figure 11. Same as Figure 9 but background density derived from adiabat calculated for Z=0.1 and Z=0.135.

consuming task of sampling the density profiles. As a second example, Figure 11 shows the residual density relative to a background adiabat with a lower value of Y = 0.1 and with heavy elements mixed in with a ratio Z = 0.135 in line with atmospheric constraints at $\sim 9 \times$ solar enrichment. This adiabat was calculated using the Militzer & Hubbard (2013) and Saumon et al. (1995) EOSs as combined by Miguel et al. (2016) to treat arbitrary H–He mixtures and ANEOS (Thompson 1990) for water ice.

The median density of the empirical models is consistent with the adiabatic density down to $r/R_{\rm m}\approx 0.95$, is somewhat lower down to $r/R_{\rm m}\approx 0.7$, then climbs again. Models in the distribution that follow these trends may be interpreted as supporting the idea of an extended stably stratified region (Fuller 2014). But, again, the median is not the distribution. To a "1 σ " level, the adiabatic density profile is consistent with the empirical samples down to at least $r/R_{\rm m}=0.35$.

As a last example, we use as our reference background the end state of a recent Saturn thermal evolution model (Mankovich & Fortney 2019). This structure derives from calculating the cooling of Saturn's interior, including the phase separation of He from H in the interior. This leaves the molecular part of Saturn's envelope depleted in He (to Y = 0.07) and the inner regions extremely He enriched $(Y \gtrsim 0.9 \text{ inside } 0.24 \lesssim s/R_{\rm m} \lesssim 0.37)$. The model includes a uniform metallicity Z = 0.048 in the envelope, with a dense Z = 1 core below $s/R_{\rm m} = 0.24$. The model matches Saturn's present-day radius and intrinsic luminosity but does not attempt to match the observed gravity field. Subtracting this background density, we again examine the residual density in the sampled profiles (Figure 12). Compared with this particular evolution model, a majority of our gravity solutions produce quite consistent densities throughout the interior of the planet. That the density residual is consistent with zero virtually everywhere in the planet indicates (1) that this rather extreme level of helium depletion in the molecular envelope is permitted by Saturn's observed gravity field, (2) that the overdensity of our models at depth ($s/R_{\rm m} \lesssim 0.2$) compared to constant-composition adiabats (Figures 9 and 11) can indeed be provided by a central core of dense material, as expected, and (3) a helium-rich shell surrounding such a core is also

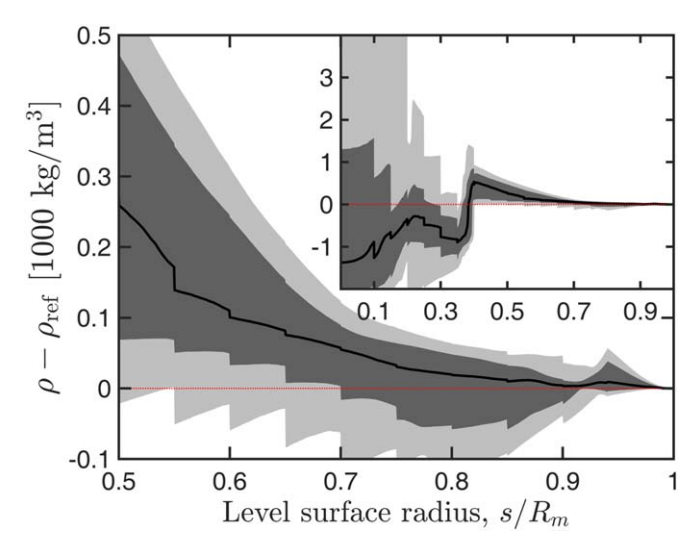


Figure 12. Same as Figure 9 but with the background density defined by the end state of an evolution model (Mankovich & Fortney 2019).

consistent with the low-order gravity field. These observations are at the 1σ - 2σ level, i.e., solutions also exist that do not follow these trends.

4. Discussion and Conclusions

In this paper, we presented an empirical approach to using gravity data to explore the interior structures of fluid planets and applied it to Saturn using data from *Cassini*'s Grand Finale orbits. Here we wish to summarize our findings for Saturn, and about planetary interior modeling in general, and to consider the strengths and weaknesses of our "density first" approach, versus traditional, composition-based modeling.

First, a point that was already made above but bears repeating: gravity data alone offer robust but loose constraints. The great variety of density profiles included in our sample may seem surprising and counterintuitive, but it is an unavoidable consequence of using an integrated quantity, in this case the external potential, to study the spatial distribution of local quantities, in this case the interior density and all properties of the planet that derive from it. Without imposing additional constraints, we necessarily obtain nonunique solutions, and this is a separate and more fundamental limitation than the problem of uncertainty in the data and/or calculation.

As a result, the main finding we can report on, with respect to Saturn, is to confirm the well-known but often underappreciated suspicion that solutions to Saturn's gravitational potential field exist that do not conform to a simple model of a few compositionally homogeneous and thermally adiabatic layers. While this may not be a surprise, it is nevertheless a previously unproven result. We could not know, a priori, whether the nonuniqueness of gravity solutions would translate to a narrow range of allowed interior structures or to a wide variety, as appears to be the case.

We can contrast this with the seemingly more informative but less robust outcomes from traditional models. These are often able to report narrow ranges for a number of key quantities (typically core mass, bulk metallicity, H/He envelope metallicity, atmospheric helium depletion) that were the free parameters in the chosen model. The trade-off for these precise, straightforward estimates is their unknown validity, being tied to very particular and often very simple a priori modeling framework for the planet.

For example, recent modeling efforts based on Cassini data and utilizing state-of-the-art EOSs have concluded that no rigidly rotating models can be found that fit the measured gravity coefficients J_2 , J_4 , and J_6 simultaneously to any reasonable precision, and have interpreted this as strong evidence for differential rotation in Saturn (Galanti et al. 2019; Iess et al. 2019). In fact, while evidence for differential rotation in Saturn is indeed strong (most notably the detection of odd harmonics J_3 and J_5), it is not true that rigidly rotating models cannot match the even harmonics. The empirical models in our sample all fit, by construction, the even gravity harmonics to the prescribed uncertainty, and we verified, by using the precise but slower CMS method, that empirical models can be constructed to match the measured measured harmonics to the full precision of the data. The existence of such models does not really prove or disprove anything of substance; what it does is illustrate the risk of drawing a general conclusion from a specific model.

4.1. Narrowing Down the Posterior Distribution

It is certainly possible that a subset of the sampled density profiles can be "disqualified" based on other physical considerations, and indeed we consider this a natural avenue for future work. Any reduction of the allowed solution space will be an improvement, as it narrows down the probable actual structure of Saturn. However, any such reductions must be considered carefully, so that they do not rely too strongly on implicit assumptions of the exact kind we decided to avoid in the first place. Such low-hanging fruit as disqualifying unphysical density inversions or density extremes had already been picked by passing an appropriate prior probability function, p(x), to the MCMC sampler (Appendix C). For instance, that is why the posterior sample does not contain profiles with stationary points or with central densities much higher than $2 \times 10^4 \text{ kg m}^{-3}$. More subtle constraints, e.g., looking for convective instabilities or checking pressuredensity pairs against known EOSs, require knowledge of the thermal state and inevitably require additional assumptions.

A second and unrelated way to narrow the predicted distribution somewhat is to "sharpen" the likelihood function by including higher-order coefficients and/or with tighter uncertainties. Recall that J_2 and J_4 are known for Saturn with better accuracy than was assumed in Equation (4). The same is true for Jupiter, and higher-order coefficients are also known, with decreasing accuracy, for both planets. More precise calculation of the Js for a given density profile can reach this level of accuracy, with the only downside being increased computation time. While this would be a worthwhile improvement, it would only be appropriate if and when the actual rotation state of Saturn is known, including any dynamical and/or non-rigid-body components, to sufficient accuracy from independent measurements. That would allow matching models of rigid rotation with an adjusted gravity measurement reflecting a known correction due to differential rotation.

Finally, our inferred heavy-element mass for Saturn relied on the SCVH EOS for H–He. This widely used EOS has been recently updated to be more thermodynamically consistent (Chabrier et al. 2019). In the updated version, hydrogen is found to be denser under Jupiter and Saturn conditions, in agreement with DFT calculations. Therefore, the heavy-element masses listed here are likely overestimates. Clearly, a more detailed investigation of that topic in the future is desirable.

What we have accomplished is an understanding of a much fuller range of interior density profiles for Saturn that are allowed by the planet's gravity field as determined by the *Cassini* Grand Finale, a data set that will likely not be surpassed for some decades. We hope that the allowed density distributions are a long-lived data product that other workers may find useful as new ideas about planetary formation, structure, and evolution emerge. Such ideas can be compared against the allowed interior density distributions that we have found here. To facilitate this, we archive the data products and analysis tools used in this study, documented in sufficient detail to allow reuse and alternative analysis. The archive can be found at https://doi.org/10.7291/D1P07G.

We would like to thank Dan Foreman-Mackey, Nadine Nettlemann, Bill Hubbard, Burkhard Militzer, Sean Wahl, Daniele Durante, and Luciano Iess for helpful advice on several aspects of this work. We thank Tristan Guillot for his thorough and thoughtful review. J.J.F. acknowledges the support of NASA *Cassini* Participating Science grant NNX16AI43G and the University of California grant A17-0633-001 to the Center for Frontiers in High Energy Density Science. Resources supporting this work were provided by the NASA High-End Computing (HEC) Program through the NASA Advanced Supercomputing (NAS) Division at Ames Research Center, as well as the lux supercomputer at UC Santa Cruz, funded by NSF MRI grant AST 1828315.

Software: emcee (Foreman-Mackey et al. 2013).

Appendix A A Single-parameter Description of the Low-pressure Region

As explained in Section 2.2, when choosing a parameterization, our goal is to find the best compromise between a simple description, with a small number of parameters suitable for MCMC sampling, and a general description, letting the resulting $\rho(s)$ curves explore all reasonable profiles. Our choice of parameterization by piecewise-quadratic functions was guided by, but is much more general than, previously published models that were based on physical EOSs and an adiabatic temperature gradient (Mankovich et al. 2019). We found that, for the bulk of the planet, a piecewise-quadratic $\rho(s)$ is able to capture the profiles derived with a physical EOS and flexibly explore beyond them.

However, empirical $\rho(s)$ profiles derived from this parameterization inevitably exhibit a small but significant deviation from profiles derived by physical models, in a small region at the top of the upper envelope. Figure 13 illustrates the problem. An inflection is seen in all the EOS-based $\rho(s)$ curves, always in the neighborhood of $s/R_m \approx 0.95$, and this inflection cannot be captured if a single polynomial is used to approximate the entire upper envelope (typically extending down to at least $s/R_m \approx 0.65$). Above the inflection point is a small region where $\rho(s)$ seems to follow a different curve. And yet, this small region of the upper envelope is one where physical models are most reliable, at a pressure and temperature region where EOSs are well tested and where an adiabatic temperature gradient is expected to exist. Closely matching the EOS-based models in this upper region of the planet is an important way in which to constrain empirical models.

The obvious solution is to add an additional segment to the piecewise-polynomial parameterization, but unfortunately this cannot be implemented. The problem is not simply that this

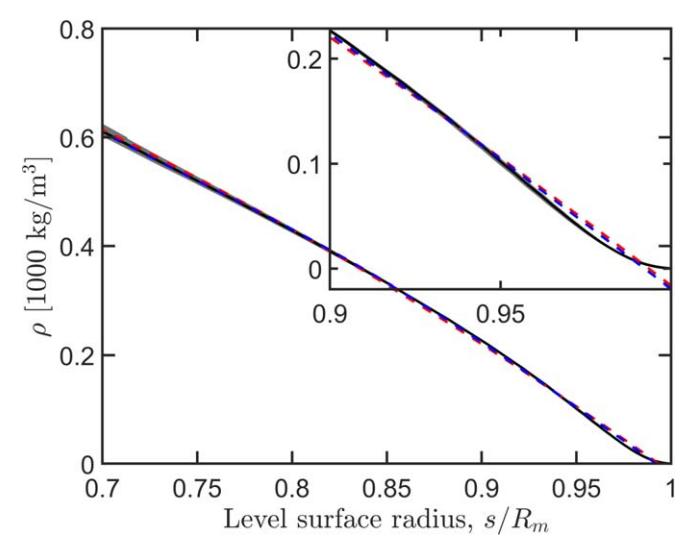


Figure 13. A close look at the upper envelope of traditional Saturn models (Mankovich et al. 2019), the same models seen in Figure 2 in the main text. The solid black curve is the ensemble median density at each radius, with the light-gray band denoting the 1σ variation. The red and blue dashed lines are best-fit polynomials of degree 2 and 4, approximating the density profile in the upper envelope as a whole. Neither is a good approximation in the small region where $s \ge 0.95R_m$.

would require five to six additional parameters and greatly complicate the sampling process. More seriously, the small region in question contains relatively little mass. Small changes in density in this region do not make a big-enough difference in the *J* values, at our level of precision, to effectively "drive" the likelihood function. There is no reason to expect then that profiles from the resulting posterior would be any more like the EOS-based ones.

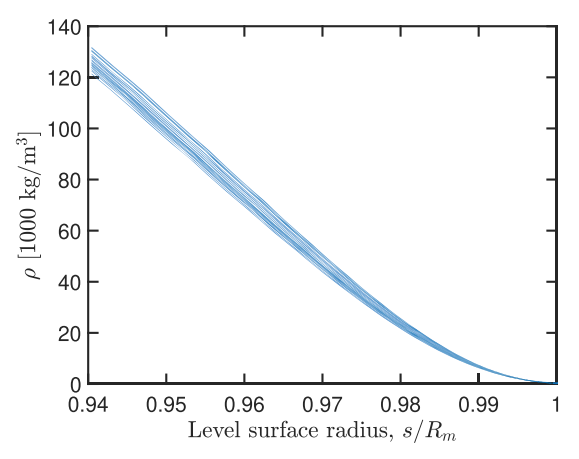
Instead, we use a more explicit constraint, ad hoc in nature, which achieves the desired result of keeping the top of the envelope in empirical models similar to EOS-based models while retaining enough flexibility to mimic varying composition.

We examine the shapes of the density profiles of M19 in the region above $z_a = s/R_m = 0.94$ (Figure 14(a)). We choose this fixed point, slightly below the inflection seen in the models, to make sure we always capture the slope accurately. For $z < z_a$, we use the main parameterization by piecewise quadratics (Equation 3 and Appendix B). Above z_a , we find that all profiles can be fit by fourth-degree polynomials (quartics) to excellent agreement. Further, if we denote $\rho_a = \rho(z_a)$, we find that, for $z_a \le z \le 1$, the curves $\rho(z)/\rho_a$ are equally well fit by quartics (not surprising), and in fact, that they can all be adequately approximated by the same quartic polynomial:

$$\frac{\rho(z_a \leqslant z \leqslant 1)}{\rho(z_a)} \approx Q(z) = (3 \times 10^4)z^4 - (1.128 \times 10^5)z^3 + (1.587 \times 10^5)z^2 - (9.914 \times 10^4)z + (2.323 \times 10^4),$$
(9)

shown in Figure 14(b). The profiles in Figure 14(a) can be recovered, approximately but with high fidelity, by multiplying the polynomial (9) by a particular value of ρ_a .

In other words, in the region $z \ge z_a$ the physical, EOS-based models form a one-parameter family of quartic functions. We do not see a special physical meaning here. It is simply that the variation in density that originated from making different choices about composition (i.e., the envelope's helium mass fraction and metallicity) under the severe but, in this region,



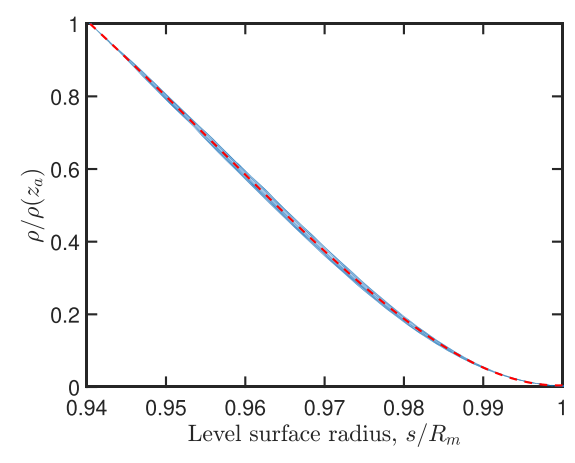


Figure 14. The same profiles as in Figure 13 truncated at $s/R_m = 0.94$, slightly below the inflection point. The apparently similar curvature motivates us to fit them all with a single quartic polynomial in $z = s/R_m$ by normalizing to the value $\rho_a = \rho(z_a = 0.94)$. This polynomial, Equation (9), together with a posterior distribution of ρ_a generate density profiles that resemble the physical models in shape but are free to explore "around" them.

well-justified adiabatic assumption, can be empirically captured by varying the value of $\rho_a = \rho(s/R_m = 0.94)$. To make sure that our empirical profiles are similar to but not overly constrained by EOS-based models in the region $z \geqslant z_a$ all we have to do is set an appropriate prior on the parameter ρ_a . Guided again by the physical models, we choose a uniform prior in the range 100 kg m⁻³ $\leqslant \rho_a \leqslant$ 200 kg m⁻³ with an exponentially decaying probability outside this range.

Appendix B Complete Definition of Parameters Sampled by MCMC

As explained in Section 2.2 of the main text, our choice of parameterization of empirical density profile is a piecewise-quadratic function. There are two breakpoints, at normalized radii z_1 and z_2 , where a jump discontinuity is explicitly allowed (but not required) and between them are three quadratic segments each defined by three parameters, for a total of 11 free parameters required to define a density profile $\rho(s)$.

There is more than one way to let three numbers define a quadratic function. In principle, all are equivalent but in practice MCMC sampling works best (i.e., converges fastest) when the parameters are minimally correlated, and the likelihood function is a smooth function of their numerical values. It is especially important to avoid likelihood "cliffs," where a small change in one parameter value results in a sudden drop in the likelihood value, perhaps because a physically motivated prior condition has been violated. This is a real danger and often leads the most intuitive and simple parameterizations to fail.

For example, defining the quadratic segments by

$$\rho(z) = \begin{cases} a_1 z^2 + b_1 z + c_1, & z_1 < z, \\ a_2 z^2 + b_2 z + c_2, & z_2 < z \le z_1, \\ a_3 z^2 + b_3 z + c_3, & z \le z_2, \end{cases}$$
(10)

would not do. The nine parameters a_i , b_i , c_i are highly correlated, meaning a small change in the value of one usually requires a simultaneous and "coordinated" change in several others to prevent the resulting density profile from changing too much and landing in a low-likelihood region. Worse, the locus of parameter values that yield physically permissible density profiles (without negative density or any density

inversions) form distinct islands in parameter space, with zero-likelihood regions between them that are practically impossible for MCMC algorithms to cross.

By trial and error, we arrive at the following alternative parameterization, admittedly complicated, but effective. In addition to z_1 and z_2 , the nine parameters defining the quadratic segments are

$$\mathbf{x} = [a_1, \, \rho_{10}, \, y_{11} = \log(\rho_{11} - \rho_{10}),
a_2, \, y_{21} = \log(\rho_{21} - \rho_{11}), \, y_{22} = \log(\rho_{22} - \rho_{21}),
a_3, \, y_{32} = \log(\rho_{32} - \rho_{22}), \, y_{33} = \log(\rho_{33} - \rho_{32})].$$
(11)

The parameters a_i control the curvature of segment i and the ρ_{ij} are the densities at the segment ends. The segments are numbered from top to bottom: segment 1 includes $z_1 < z \le z_a = 0.94$, segment 2 includes $z_2 < z \le z_1$, and segment 3 includes $0 < z \le z_2$. (See Appendix A for why the top segment extends up to z_a instead of z = 1.)

Next, $\rho_{10} = \rho(z_a)$ (top of segment 1) and $\rho_{11} = \lim_{z \to z_1^+} \rho(z)$ is the right-limit density at z_1 (i.e., bottom of segment 1). Similarly, $\rho_{21} = \lim_{z \to z_1^-} \rho(z)$ is the left-limit density at z_1 (top of segment 2) and $\rho_{22} = \lim_{z \to z_2^+} \rho(z)$ is the right-limit density at z_2 (bottom of segment 2). Finally, $\rho_{32} = \lim_{z \to z_2^-} \rho(z)$ is the left-limit density at z_2 (top of segment 2) and $\rho_{33} = \rho(z=0)$ is the density at the bottom of segment 3, the center of the planet.

The use of the curvature-and-endpoints description is less familiar but more intuitive than the well-known polynomial coefficients representation. Notice that the endpoint density values are defined implicitly—the actual parameter values are the log of the difference of neighboring density values. This transformation is a common MCMC "trick." It allows the sampled parameters to have values in the range $[-\infty, \infty]$ and keeps the corresponding physical parameters in their meaningful range. All values of y_{ij} are permissible and lead to physical, monotonically decreasing density profiles. Larger values of y_{21} and y_{32} lead to more pronounced density jumps between segments, while more negative values result in the jumps disappearing and the segments merging into one. Thus, all possibilities from the canonical, sharp envelope-envelope and core-envelope transitions to a completely smooth density profile throughout are representable and reachable by a continuous variation of parameter values.

The density profile itself is constructed from the parameters by solving for the polynomial coefficients that reproduce the endpoint densities: $\rho_a = \rho(z_a = 0.94)$ that we use to keep the density in the low-pressure region of the envelope compatible with values derived in traditional, EOS-based models. Guided by the models

$$\rho(z) = \begin{cases}
a_1(z^2 - z_a^2) + \left[\frac{\rho_{11} - \rho_{10}}{z_1 - z_a} - a_1(z_1 + z_a)\right](z - z_a) + \rho_{10}, & z_1 < z \leqslant z_a, \\
a_2(z^2 - z_1^2) + \left[\frac{\rho_{22} - \rho_{21}}{z_2 - z_1} - a_2(z_2 + z_1)\right](z - z_1) + \rho_{21}, & z_2 < z \leqslant z_1, \\
a_3(z^2 - z_2^2) + \left[\frac{\rho_{33} - \rho_{32}}{0 - z_2} - a_3(0 + z_2)\right](z - z_2) + \rho_{32}, & 0 < z \leqslant z_2.
\end{cases} \tag{12}$$

The prior probabilities set for the above parameters and the resulting posterior chains are given in Appendix C.

Appendix C Sampling Procedure

The full list of parameters we need to explore is

$$\mathbf{x} = \{m_{\text{rot}}, a_1, y_{10}, y_{11}, a_2, y_{21}, y_{22}, y_{32}, y_{33}, z_1, z_2\}.$$
 (13)

See Appendix B for the meaning of these parameters. Notice that a_3 is apparently missing from the list above. In fact, as explained in Section 2.5, the requirement that $\lim_{s\to 0^+} d\rho(s)/ds = 0$ constrains the innermost segment of $\rho(s)$ such that only two parameters are independent. The curvature of that segment follows

$$\rho_{10} = y_{10},
\rho_{11} = \rho_{10} + \exp(y_{11}),
\rho_{21} = \rho_{11} + \exp(y_{21}),
\rho_{22} = \rho_{21} + \exp(y_{22}),
\rho_{32} = \rho_{22} + \exp(y_{32}),
\rho_{33} = \rho_{32} + \exp(y_{33}),
a_3 = \frac{(\rho_{32} - \rho_{33})}{z_2^2}.$$
(14)

In Section 2.5, we explain that the high degree of correlation between the variables in Equation (13) makes it very difficult to sample from the full posterior simultaneously. We find it necessary to sample instead from the conditional probabilities, $p_z = p(\mathbf{x}'|\mathbf{Z} = \mathbf{z})$, where $\mathbf{Z} = \{z_1, z_2\}$ and $\mathbf{x}' = \mathbf{x} \setminus \mathbf{Z}$. In words: we fix values for the radii z_1 and z_2 , and sample the remaining 10 parameters, resulting in a conditional distribution. We repeat this for many values of z_i to build a picture of the full posterior.

B.1. Prior Probabilities of Sampled Parameters

The prior for x is a product of independent priors for each component. The rotation prior is $m_{\rm rot} \sim \mathcal{N}(0.14224, 4.5 \times 10^{-4})$. The mean corresponds to a rotation period of $10^{\rm h}33^{\rm m}30^{\rm s}$ and the deviation is about 1 minute.

The curvature parameters take a uniform prior $a_i \sim \mathcal{U}(-3 \times 10^6, 3 \times 10^6)$. These limits do not have a special physical meaning; they are reasonable bounds we find by experimentation.

The parameter $y_{10} = \rho_a$ has a particularly important prior. Recall that this is a density at a reference point

presented in Mankovich et al. (2019) we set¹⁴

$$\log p(y_{10}) \sim -\frac{1}{2} \left(\frac{100 - \min(y_{10}, 100)}{10} + \frac{\max(y_{10}, 200) - 200}{10} \right)^{2}, \tag{15}$$

and the numerical values are in kg m $^{-3}$. In words: it is a uniform probability inside the 100 to 200 kg m $^{-3}$ range with exponentially decaying probability outside of it with an e-folding distance of 10 kg m $^{-3}$.

The other y_{ij} parameters are logarithms of density differences. They can take positive or negative values, and the values get exponentiated and added to define the densities at the endpoints of the quadratic segments, ρ_{ij} . It is natural to define the prior on the actual density values, say a uniform prior in the 0–30,000 kg m⁻³ range (merely a guess as to the highest density achievable in Saturn). We need to be careful though. The transformation from ρ_{ij} to y_{ij} involves a transformation of the probability; the prior on y_{ij} is not uniform. Instead, it follows from the conservation of probability mass in equivalent parts of the distribution: $p_{\rho}(\rho')d\rho' = p_{y}(y')dy'$. The answer is $y_{ij} \sim e^{y'}\mathcal{U}(-\infty, \infty)$, but it helps to cut off the uniform probability outside of a reasonable range. The final prior therefore is

$$\log p(y_{ij}) \sim \begin{cases} y_{ij} & -20 < y_{ij} < 12, \\ -\infty & \text{otherwise.} \end{cases}$$
 (16)

There is no prior on z_1 and z_2 because they are not MCMC sampled.

B.2. Sampling from the Conditional Distributions

We obtain a sample from p_z for each pair $\{z_1, z_2\} \in \{0.35, 0.4, 0.45, ..., 0.9\} \times \{0.1, 0.15, 0.2, ..., 0.4\}$ subject to the condition $z_1 > z_2$. There are 81 pairs and thus 81 separate MCMC runs to produce samples from the different conditional distributions. We use the implementation of ensemble sampling

¹⁴ Happily, we never have to worry about normalizing the probability as only probability ratios (actually log-probability differences) are ever used.

probability ratios (actually log-probability differences) are ever used. ¹⁵ There are, after all, a lot of numbers available between, say, -20 and $-\infty$ that as logarithms all mean simply: $\Delta \rho = 0$.

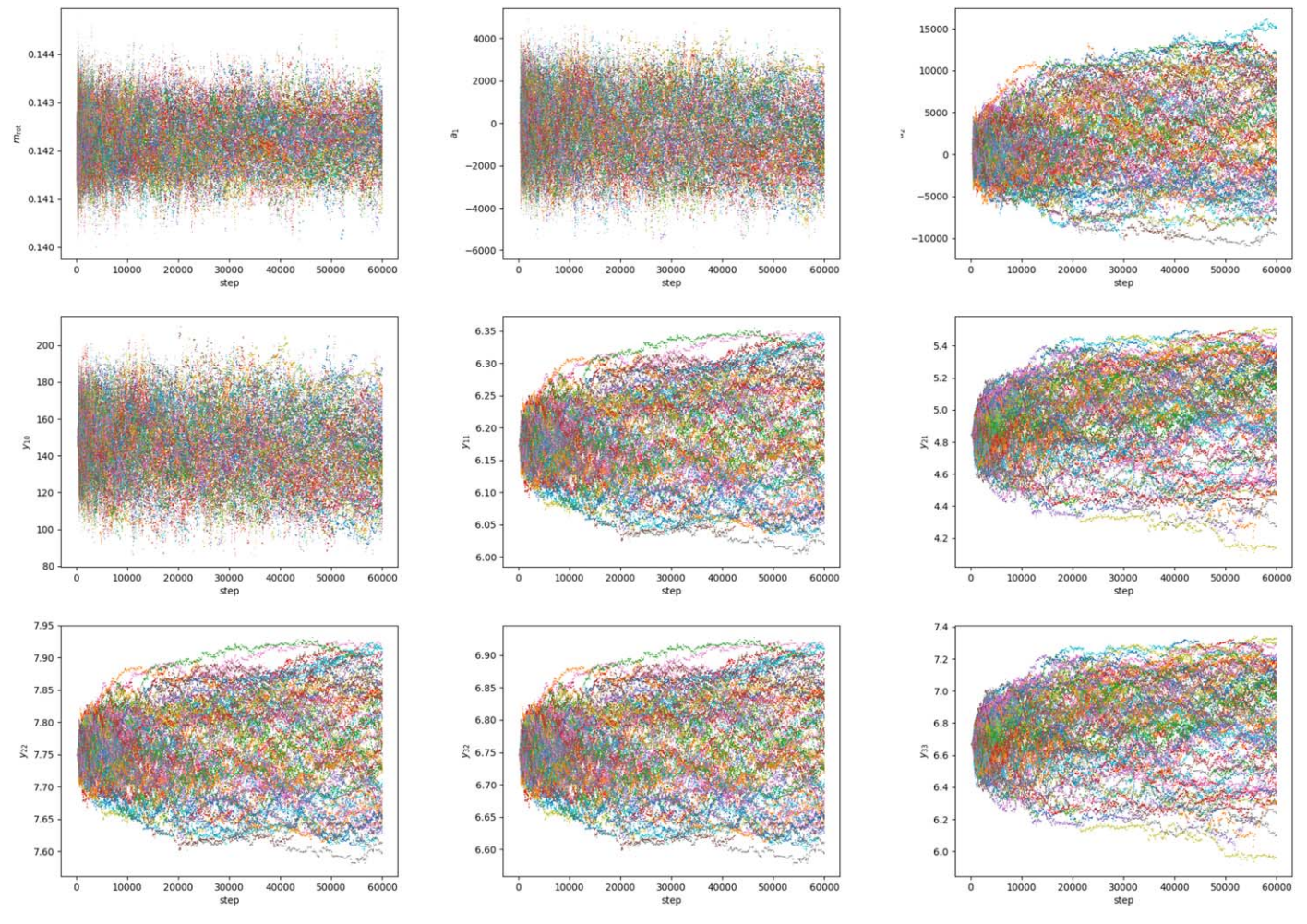


Figure 15. Trace plots from MCMC run with $z_1 = 0.65$ and $z_2 = 0.2$.

in emcee, with the default stretch-move algorithm, and run 78 walkers for 60,000 steps each.

Trace plots for one such MCMC run are shown in Figure 15; similar behavior is exhibited in all runs. Visual inspection of trace plots is one method of deciding what part of the MCMC chain we can use to take independent samples from. Inspection of Figure 15 reveals why we had to use many walkers for so many steps. Several of the parameters exhibit slow mixing, taking more than 30,000 steps to fully forget their seed state. Even worse than the long burn-in time is the low acceptance rate, which leads to quite long autocorrelation in many dimensions. In other words, successive steps are not independent, requiring about 200 steps to become uncorrelated. This means that an MCMC run evaluating more than 4.5 million candidate models produces only about 10,000 usable ones.

It is common practice to display the results of MCMC sampling in a series of series of two-dimensional histograms of parameter pairs. This visualization, often called a corner plot, is a convenient way to quickly make sense of the distribution of parameters including the relationships between them. In our case, the parameters are too far removed from a physical meaning for us to derive any useful insight from their pairwise histograms. We include the corner plot for one MCMC run anyway, in Figure 16.

B.3. Combining the Conditional Probabilities into a Single Posterior

After culling the MCMC chains, we have what we hope are independent samples from the conditional probabilities p_z . Next, we need to combine subsets from these samples in a way that approximates a sample from the full posterior, p(x). This task is similar to the *model selection* problem of Bayesian inference. We have found parameter distributions for different statistical models, and we wish to use this information to evaluate the relative likelihood between the models, in our case between interior profiles with different locations of discontinuous density. If we know the relative likelihoods, we can combine subsets from the individual models in proportion to their likelihood to obtain our posterior sample.

Although this is a common and well-studied task, it is nevertheless a difficult one, and there is no known best method or even useful error bounds. Nelson et al. (2018) report on a thorough comparison of many different approaches to this problem (often referred to as calculating the posterior odds or the Bayes factor or the evidence integral or simply the evidence), including the method we chose, which is based on calculating the Bayes Information Criterion, or BIC:

$$BIC(z) = -2\log(\max_{\mathbf{x}}(p_{\tau}(\mathbf{x}'))) + \log N, \tag{17}$$

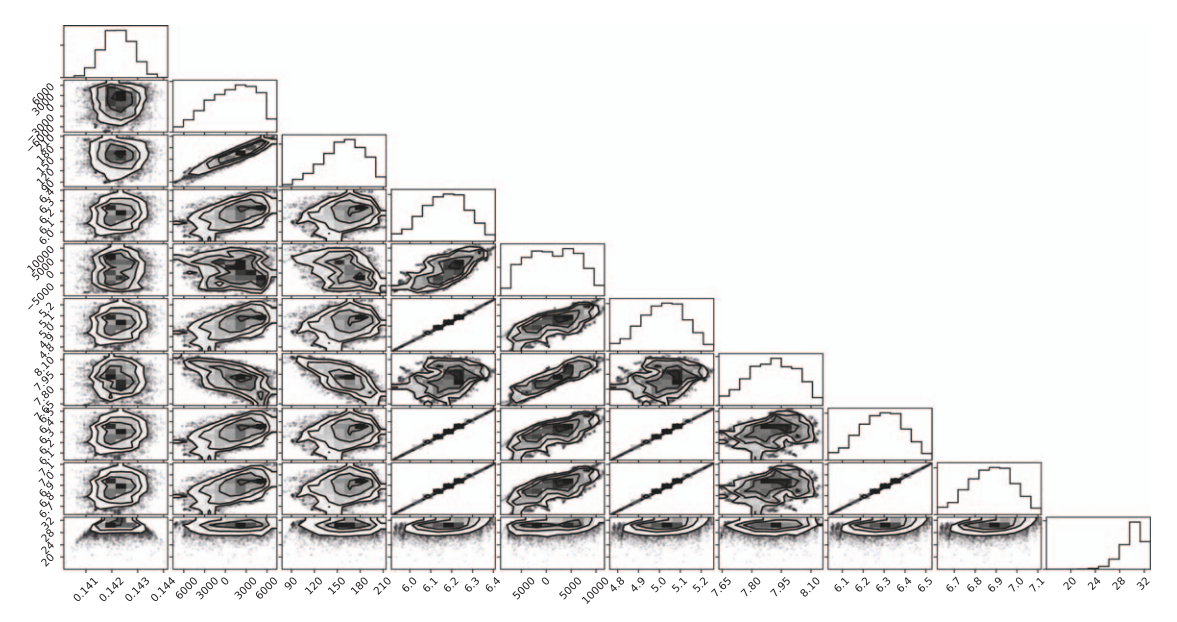


Figure 16. Corner plot of parameters sampled for the $z_1 = 0.65$ $z_2 = 0.2$ conditional probability (same run as Figure 15), after discarding the first 30,000 steps from each walker and thinning the rest by keeping one in every 200 steps. The subplot in the *i*th row and *j*th column is the two-dimensional histogram of parameters *i* and *j*, as ordered in Equation (13).

where k is the number of model parameters and N is the number of data points. The relative likelihood is given by

$$\frac{p_{z_a}}{p_{z_b}} = \exp(-(BIC_{z_b} - BIC_{z_a})/2). \tag{18}$$

In our case, k=9 always and $N\approx 10^4$, and the maximum likelihood is likewise very similar between all 81 conditional samples. So, it happens that the pairwise relative likelihood among all the conditional distributions is close to one. We take random draws from the 81 conditional samples, in almost equal proportions, to obtain a single set of 20,000 hopefully independent draws from the unknown posterior, p(x|OBS). Histograms of the 12 parameters (including a_3 , which is not sampled but uniquely determined by Equation (14)) are shown in Figure 17. These are the parameters used to reconstruct the density profiles shown in Figure 3 and to perform the analysis in the rest of the paper.

Finally, the distribution of empirical models from our sample in the $J_2 - J_4$ and $J_4 - J_6$ planes is shown in Figure 18. In many previous works that use the gravity field to study the planetary interior, this is a central result and a similar plot would be a prominent figure in the main text. In the traditional modeling approach, this is a useful indication of how the variation of model parameters (which in traditional models have important physical meaning) translates to variation in the model's gravity. In our empirical, MCMC-driven study, however, this distribution is much less informative. Recall that the sampling algorithm is driven by a likelihood function that compares model values of J_i with observed values. Unless there is a bug in the implementation, the J_i distribution in the final sample is determined entirely by the choice of likelihood function and tells us nothing about the underlying model. Nonetheless, we include this figure to potentially help a direct comparison with past or future investigations.

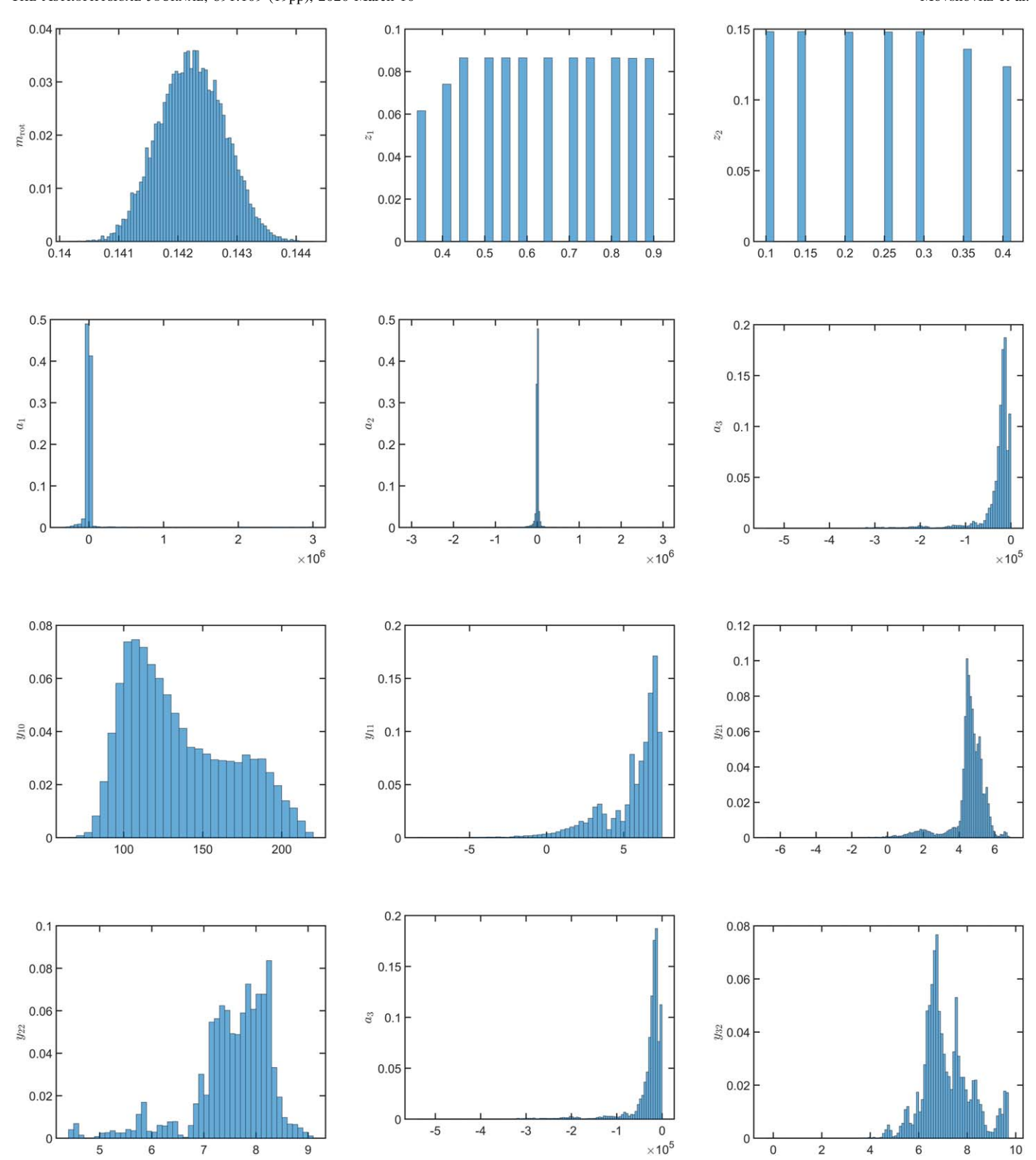


Figure 17. Histograms of parameter values used to construct the density profiles used in this work.

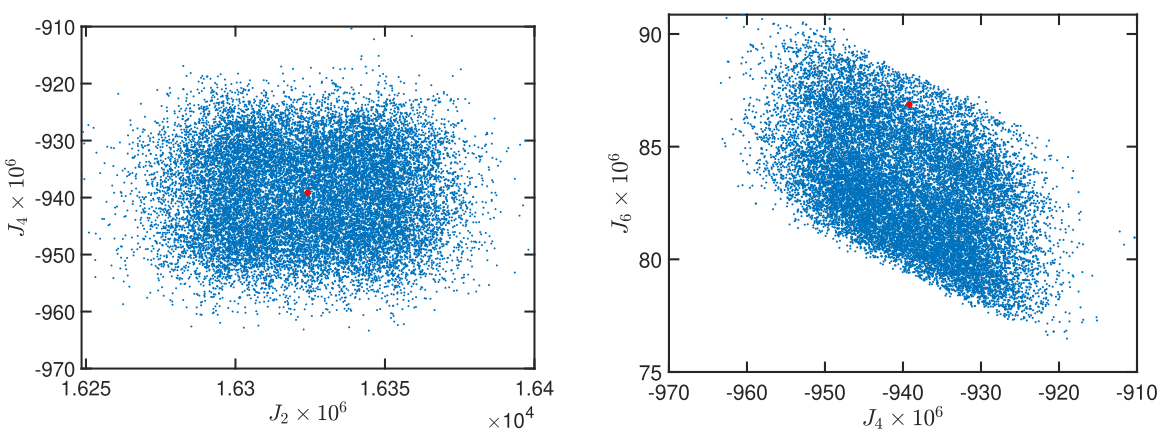


Figure 18. Gravitational harmonics of the empirical models of Figure 3 of the main text. The coefficients for Saturn's observed gravity (Iess et al. 2019) are indicated by a red circle.

ORCID iDs

Naor Movshovitz https://orcid.org/0000-0001-5583-0042 Jonathan J. Fortney https://orcid.org/0000-0002-9843-4354 Chris Mankovich https://orcid.org/0000-0002-4940-9929 Daniel Thorngren https://orcid.org/0000-0002-5113-8558 Ravit Helled https://orcid.org/0000-0001-5555-2652

References

```
Atreya, S. K., Crida, A., Guillot, T., et al. 2016, arXiv:1606.04510
Chabrier, G., Mazevet, S., & Soubiran, F. 2019, ApJ, 872, 51
Cowles, M. K., & Carlin, B. P. 1996, J. Am. Stat. Assoc., 91, 883
Debras, F., & Chabrier, G. 2019, ApJ, 872, 100
Desch, M. D., & Kaiser, M. L. 1981, GeoRL, 8, 253
Foreman-Mackey, D., Hogg, D. W., Lang, D., & Goodman, J. 2013, PASP,
Fortney, J. J., Helled, R., Nettelmann, N., et al. 2018, in Saturn 21st Century,
  ed. K. H. Baines et al. (Cambridge: Cambridge Univ. Press), 44
Fortney, J. J., & Hubbard, W. B. 2003, Icar, 164, 228
French, M., Mattsson, T. R., Nettelmann, N., & Redmer, R. 2009, PhRvB, 79,
Fuller, J. 2014, Icar, 242, 283
Galanti, E., & Kaspi, Y. 2017, ApJL, 843, L25
Galanti, E., Kaspi, Y., Miguel, Y., et al. 2019, GeoRL, 46, 616
Goodman, J., & Weare, J. 2010, CAMCS, 5, 65
Guillot, T., Miguel, Y., Militzer, B., et al. 2018, Natur, 555, 227
Helled, R. 2011, ApJL, 735, 16
Helled, R., Anderson, J. D., Podolak, M., & Schubert, G. 2011a, ApJ, 726, 15
Helled, R., Anderson, J. D., Schubert, G., & Stevenson, D. J. 2011b, Icar,
   216, 440
Helled, R., Galanti, E., & Kaspi, Y. 2015, Natur, 520, 202
Helled, R., & Guillot, T. 2013, ApJ, 767, 113
Helled, R., Schubert, G., & Anderson, J. D. 2009, Icar, 199, 368
Helled, R., & Stevenson, D. J. 2017, ApJL, 840, L4
Hubbard, B. 2013, ApJ, 768, 43
Hubbard, W. 2012, ApJL, 756, L15
Hubbard, W. B. 1982, Icar, 52, 509
Hubbard, W. B., Podolak, M., & Stevenson, D. J. 1995, in Neptune Trit., ed.
   D. P. Cruikshank, M. S. Matthews, & A. M. Schumann (Tucson, AZ: Univ.
   Arizona Press), 109
```

```
Iess, L., Militzer, B., Kaspi, Y., et al. 2019, Sci, 2965, eaat2965
Jacobson, R. A., Antreasian, P. G., Bordi, J. J., et al. 2006, AJ, 132, 2520
Kaspi, Y., Galanti, E., Iess, L., & Durante, D. 2018, AAS/DPS Meeting
   Abstracts, 50, 500,07
Kaspi, Y., Showman, A. P., Hubbard, W. B., Aharonson, O., & Helled, R.
  2013, Natur, 497, 344
Leconte, J., & Chabrier, G. 2012, A&A, 540, A20
Ledoux, P. 1947, ApJ, 105, 305
Lindal, G. F., Sweetnam, D. N., & Eshleman, V. R. 1985, AJ, 90, 1136
Mankovich, C., Fortney, J. J., & Moore, K. L. 2016, ApJ, 832, 113
Mankovich, C., Marley, M. S., Fortney, J. J., & Movshovitz, N. 2019, ApJ,
Mankovich, C. R., & Fortney, J. J. 2020, ApJ, 889, 51
Marley, M. S., Gomez, P., & Podolak, M. 1995, JGR, 100, 23349
Mazzola, G., Helled, R., & Sorella, S. 2018, PhRvL, 120, 25701
Miguel, Y., Guillot, T., & Fayon, L. 2016, A&A, 596, 114
Militzer, B., & Hubbard, W. B. 2013, ApJ, 774, 148
Militzer, B., Soubiran, F., Wahl, S. M., & Hubbard, W. B. 2016, JGRE,
   121, 1552
Militzer, B., Wahl, S., & Hubbard, W. B. 2019, ApJ, 879, 78
Morales, M. A., Schwegler, E., Ceperley, D. M., et al. 2009, PNAS, 106, 1324
Nelson, B. E., Ford, E. B., Buchner, J., et al. 2018, arXiv:1806.04683
Nettelmann, N. 2017, A&A, 606, 139
Nettelmann, N., Fortney, J. J., Moore, K. L., & Mankovich, C. 2015, MNRAS,
   447, 3422
Nettelmann, N., Holst, B., Kietzmann, A., et al. 2008, ApJ, 683, 1217
Nettelmann, N., Püstow, R., & Redmer, R. 2013, Icar, 225, 548
Podolak, M., Helled, R., & Schubert, G. 2019, MNRAS, 487, 2653
Podolak, M., Podolak, J., & Marley, M. 2000, P&SS, 48, 143
Read, P. L., Dowling, T. E., & Schubert, G. 2009, Natur, 460, 608
Saumon, D., Chabrier, G., & van Horn, H. M. 1995, ApJS, 99, 713
Schöttler, M., & Redmer, R. 2018, PhRvL, 120, 115703
Stevenson, D. 1985, Icar, 62, 4
Stevenson, D. J. 1975, PhRvB, 12, 3999
Stevenson, D. J., & Salpeter, E. E. 1977, ApJS, 35, 221
Thompson, S. L. 1990, ANEOS Analytic Equations of State for Shock Physics
  Codes Input Manual, Tech. Rep., Albuquerque, NM: Sandia National
Vazan, A., Helled, R., & Guillot, T. 2018, A&A, 610, 14
Vazan, A., Helled, R., Podolak, M., & Kovetz, A. 2016, ApJ, 829, 118
Wahl, S. M., Hubbard, W. B., Militzer, B., et al. 2017, GeoRL, 44, 4649
Zharkov, V. N., & Trubitsyn, V. P. 1978, Physics of Planetary Interiors
   (Tucson, AZ: Pachart Publishing)
```